Resting-state cross-frequency coupling networks in human electrophysiological recordings

Short title: Resting-state cross-frequency coupling networks

Felix Siebenhühner[1,2,3], Sheng H Wang[1,2], Gabriele Arnulfo[1,4], Lino Nobili[5,6], J. Matias Palva[1,7,*], Satu Palva[1,7,*]

[1] Neuroscience Center, HiLife (Helsinki Institute of Life Science), University of Helsinki, Finland

[2] Doctoral Program Brain & Mind, University of Helsinki, Finland

[3] BioMag Laboratory, HUS Medical Imaging Center, Helsinki, Finland

[4] Dept. of Informatics, Bioengineering, Robotics and System engineering, University of Genoa, Genoa, Italy

[5] Child Neuropsychiatry Unit, IRCCS, Istituto G. Gaslini, Department of Neuroscience (DINOGMI), University of Genoa, Italy

[6] "Claudio Munari" Epilepsy Surgery Centre, Niguarda Hospital, Italy

[7] Centre for Cognitive Neuroimaging, Institute of Neuroscience & Psychology, University of Glasgow, United Kingdom

* to whom correspondence should be addressed:

satu.palva@helsinki.fi or matias.palva@helsinki.fi

JMP and SP contributed equally.

Abstract

Neuronal oscillations underlie temporal coordination of neuronal processing and their synchronization enables neuronal communication across distributed brain areas to serve a variety of sensory, motor, and cognitive functions. The regulation and integration of neuronal processing between oscillating assemblies at distinct frequencies, and thereby the coordination of distinct computational functions, is thought to be achieved via cross-frequency coupling (CFC). Although many studies have observed CFC locally within a brain region during cognitive processing, the large-scale networks of CFC have remained largely uncharted. Critically, also the validity of prior CFC observations and the presence of true neuronal CFC has been recently questioned because non-sinusoidal or non-zero-mean waveforms that are commonplace in electrophysiological data cause filtering artefacts that lead to false positive CFC findings. We used a unique dataset of stereo-electroencephalography (SEEG) and source-reconstructed magnetoencephalography (MEG) data to chart whole-brain CFC networks from human resting-state brain dynamics. Using a novel graph theoretical method to distinguish true inter-areal CFC from potentially false positive CFC, we show that the resting state is characterized by two separable forms of true inter-areal CFC: phase-amplitude coupling (PAC) and *n:m*-cross-frequency phase synchrony (CFS). PAC and CFS large-scale networks coupled prefrontal, visual and sensorimotor cortices, but with opposing anatomical architectures. Crucially also directionalities between low- and high-frequency oscillations were opposite between CFS and PAC. We also found CFC to decay as a function of distance and to be stronger in the superficial than deep layers of the cortex. In conclusion, these results provide conclusive evidence for the presence of two forms of genuine inter-areal CFC and elucidate the large-scale organization of CFC resting-state networks.

Keywords: Cross-frequency synchrony, MEG, SEEG, oscillations, phase synchrony, spurious connections

Introduction

Human electrophysiological activity is characterized by neuronal oscillations, *i.e.*, rhythmic excitability fluctuations at wide range of frequencies from 0.01 to over 100 Hz. Synchronization of these oscillations across brain areas coordinates provides a mechanism for regulating anatomically distributed neuronal processing (1-3). In humans, large-scale oscillatory networks of phase synchrony (PS) characterize magnetoencephalography (MEG) and stereo-electroencephalography (SEEG) data during resting state (RS) activity (4-7) and in many cognitive functions (4,7-15) at several frequencies. Oscillatory electrophysiological resting-state networks (RSNs) recorded with MEG are organized partially in a similar fashion as the RSNs observed with fMRI (16-18), these correlations being largest in the alpha (8-15 Hz, α) and beta (15-30 Hz, β) (18,19) bands. During task performance, α and β oscillations are thought to regulate through inter-areal synchronization the top-down or feed-back modulation of bottom-up sensory processing achieved in the gamma-band (γ, 30–100Hz) rhythms (20-24).

The interplay and coordination between multiple neuronal oscillations at distinct frequencies is thought to be regulated via cross-frequency coupling (CFC): phase-amplitude coupling (PAC) (25-34) and cross-frequency phase synchrony (CFS**)** (4,35-39), also known as *n*:*m*-phase synchrony (35). PAC indicates the correlation between the amplitude envelope of a faster oscillation and the phase of a slower oscillation, whereas CFS is a form of phase synchronization defined by a stable phase-difference between oscillations having an integer *n:m* frequency ratio (Figure 1a). PAC is thought to reflect the regulation of sensory information processing achieved in γ-frequencies by excitability fluctuations imposed by θ and α oscillations (40-47). On other hand, CFS can be exploited to achieve temporally precise coordination of processing and to establish spike-timing relationships among functionally distinct oscillations and networks (43,47,48). A large number of studies have identified local PAC, i.e., PAC observed between different frequencies of the same signal, between the phases of δ, θ and α oscillations and the amplitude of gamma oscillations in local field potentials (LFPs) in rats (49-55) and in human intracranial EEG (27,28,34,56,57) and MEG data (33,46,58). Similarly to PAC, local CFS has been observed in human MEG and EEG data during rest (4,8,37,59) and attentional and working memory (WM) tasks (4,36,60,61) as well as in LFPs in the rat hippocampus (52,54,62).

Despite extensive literature on local CFC, only a few studies have identified inter-areal PAC or CFS in M/EEG data between sensors (4,36,63) or between brain regions in source-reconstructed data (31,32,39,64) or intracranial recordings (38,65). Overall, the large-scale organization of CFC networks has remained largely uncharted and the roles that CFC play in linking within-frequency phase-coupled or amplitude-correlated networks have remained unknown. Furthermore, several lines of recent research have raised concerns over the possibility that estimates of CFC may be inflated by false positive couplings. Such spurious observations are readily caused by the higher-frequency filter artefacts arising from non-sinusoidal signal components (66-72) as well as by amplitude fluctuations of oscillations with non-zero-mean waveforms that lead to artificial lower-frequency oscillations during filtering (73). Both non-sinusoidal and non-zero-mean waveforms are ubiquitous in electrophysiological signals and thus the artificially generated high- and low-frequency, respectively, signal components constitute a significant confounder to CFS and PAC estimation. Hence, the validity of prior CFC observations has been questioned and therefore it is not established whether neuronal activity is characterized by true neuronal CFC rather than by spurious CFC connections. Since CFC is thought to be a central mechanism of coordinating processing across oscillations at distinct frequencies specifically during cognitive tasks and behaviors, it is crucial to establish if true neuronal CFC can be observed in neuronal activity.

In this study, we used both human SEEG and source-reconstructed MEG data to characterize the large-scale CFC networks during RS. To this end, we estimated the whole-brain connectomes of CFS and PAC and mapped their anatomical and topological structures as well as the laminar structure from SEEG data. To remove the putatively false positive CFC connections, we advanced a novel graph-theory based approach. The core tenet of CFC is that it indicates an interaction between two distinct neuronal processes. Conversely, analyses of non-sinusoidal signal properties rely on the assumption that a single underlying process generates the signal. Filter-artefact-caused spurious cross-frequency coupling cannot be dissociated from true cross-frequency coupling of two neuronal processes by an inspection or analysis of the waveform shape of any single signal in isolation (8), which essentially excludes the usage of local CFC estimates in this research. However, CFC is *necessarily* true when there is evidence for two processes, such as when CFC is found between two separable sources and the contributions of local CFC can be excluded. Building on this notion, we developed a conservative test for whether CFC is true, which is based on connection-by-connection testing of whether CFC can unambiguously be attributed to two separable processes.

Using this approach, we identified the fractions of true inter-areal CFS and PAC observable in human resting-state activity in SEEG and source-reconstructed MEG data and assessed the large-scale structures of these true-CFC connectomes. We found that two distinct forms of true inter-areal CFC, CFS and PAC characterize the human RS. CFS and PAC RSNs showed similarities to resting-state PS networks, and directional coupling in large-scale networks of the prefrontal, medial, visual and sensorimotor cortices, but crucially with distinct spectral profiles and opposing directionalities. These results support the assumptions that CFS and PAC are distinct processes for the integration of neuronal oscillatory activity across frequencies.

Results

True neuronal CFS and PAC characterize resting-activity in SEEG and MEG

Our objectives were to assess the presence of CFC in human resting-state brain activity and to characterize the putative large-scale CFC networks measured at meso-scale resolution with SEEG and at macro-scale with source-reconstructed MEG data. Large-scale CFC networks were derived from contact-to-contact (SEEG) or parcel-to-parcel (MEG) connectivity matrices where the pairwise CFC was estimated between the low-frequency (LF) time series from the one contact/parcel and the high-frequency time series from the other.

In order to systematically address the possibility that observations of CFC might be spuriously caused by filtering artefacts stemming from non-sinusoidal or non-zero-mean waveforms, we advance here a new method to control for the spurious connections. The core assumption behind CFC is that the interaction is observed between two distinct processes whereas spurious CFC is a property of a single signal with signal components distributed to the two studied frequency bands as filter-artefacts from non-sinusoidal or non-zero-mean signal properties. We set out to dissociate the two-separable-signals vs. one-signal hypotheses through a conservative network-motif test that assesses whether the two CF-coupled signals are also coupled via local CFC and inter-areal within-frequency coupling. The presence of such a "secondary connection" implies the possibility of the inter-areal CFC being spurious while a lack of such a connection indicates that the CFC cannot be attributable to a single source and is hence true.

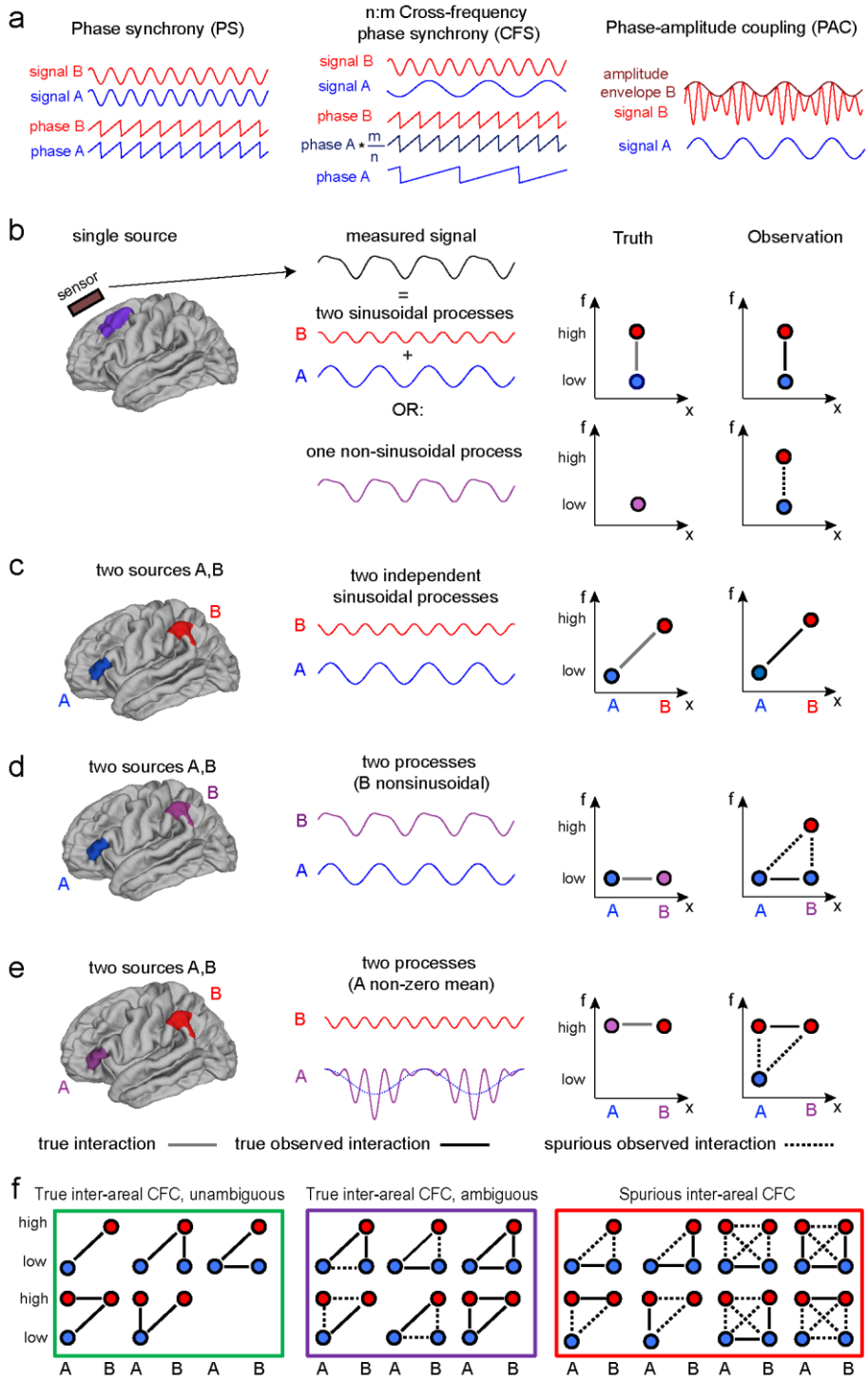

Figure 1. Schematics of true and spurious observations of inter-areal cross-frequency coupling

a) Schematic illustration of phase synchrony (PS), *n*:*m* cross-frequency phase synchrony (CFS) and phase-amplitude coupling (PAC). In PS, two spatially distant processes oscillating at the same frequency exhibit a constant phase relationship. In CFS, a constant *n*:*m* phase relationship exists between two processes at frequencies f_1, f_2 where f_1: = *m*:*n*. These processes can either take place in the same region (local CFS) or in distinct regions (inter-areal CFS). In PAC, the amplitude of the high-frequency signal is correlated with the phase of the low-frequency signal. Like CFS, PAC can be either local or inter-areal. **b)** Observations of local cross-frequency coupling (CFC) can be either true or spurious. A measured signal from a single sensor or electrode can either be the sum of two sinusoidal processes oscillating at distinct frequencies or a single non-sinusoidal process. Local CFC can be observed either when there is a true coupling between two sinusoidal processes, or from a single non-sinusoidal signal.

c) True inter-areal CFC between two spatially distant sinusoidal processes A and B. **d)** Example of spurious observation of inter-areal CFC. Process A is sinusoidal, but B is non-sinusoidal and spurious local CFC will be observed at location B, as shown in b). If A and B are connected by low-frequency PS, also spurious inter-areal CFC will be observed between A and B. **e)** Example of spurious observation of inter-areal CFC. Process B is sinusoidal, but A is non-zero-mean and spurious local CFC will be observed at location A. If A and B are connected by high-frequency PS, also spurious inter-areal CFC will be observed between A and B. **f)** Possible observations of inter-areal CFC between A and B leading to the observation of true or spurious inter-areal CFC. In cases where inter-areal CFC is not part of a full triangle motif, it is unambiguously true (green box). In cases where inter-areal CFC is spurious (red box), it is part of a full triangle motif of PS, local CFC and inter-areal CFC. However, there may also be ambiguous cases where inter-areal CFC is true, but still a full triangle motif exists (purple box).

Figure 1 shows schematically the generation of true and spurious observations of CFC as well as our approach for identifying the true and for discarding the putatively spurious observations. For local CFC, that is measured between different frequency components at one location, it is impossible to distinguish between true and spurious observations (Figure 1b), whereas this is possible for inter-areal CFC that is true if it is found between signals that unambiguously originate from separable neuronal processes (Figure 1c). We thus begin with all observations of inter-areal CFC and to safeguard against indirect leakage of local CFC into the estimates of inter-areal CFC, we exclude observations of inter-areal CFC between sources that are also connected by both local CFC and inter-areal 1:1 PS (or amplitude correlation in the case of the high-frequency signal in PAC) (see Figure 1d, e). It is notable that true neuronal CFS might also be present under these conditions (see Figure 1f, purple box) but cannot be distinguished from actual spurious CFS connections (Figure 1f, red box). Thus, the proposed method gives a conservative estimate of the presence of true neuronal CFS (Figure 1f, green box).

We mapped the connectomes of CFC and used this approach to identify and discard all putatively spurious CFC observations. We estimated the local and inter-areal cross-frequency coupling (CFC), as well as inter-areal 1:1 phase synchrony (PS) and amplitude envelope correlations (AC) using eyes-open resting-state MEG recordings (10 min) from 23 healthy controls and eyes-closed resting-state SEEG recordings (10 min) from 59 epileptic patients (see S1 Figure and S2 Figure for the analysis workflow). During preprocessing, we excluded artefacts and SEEG electrode contacts located in the epileptic zone, and filtered broadband time series into narrow frequency bands from 1 to 315 Hz (see Methods I-IV). MEG data were source-reconstructed (see Methods V-VI) and collapsed onto 200 cortical parcels of a parcellation based on the Destrieux atlas (74), of which the least reliably parcels and connections were excluded (see Methods VII-VIII). Visual inspection of

raw ongoing SEEG and MEG data between regions and frequencies that showed high coupling on average over the whole time period revealed intermittent periods of strong interareal CFS (S3 Figure) and PAC (S4 Figure) between signals that were not significantly 1:1 coupled and did not exhibit local CFS.

Inter-areal CFC for low frequencies 1–95 Hz and ratios 1:2–1:7, as well as PS and AC were estimated pair-wise between electrode contacts or parcels (see Methods IX-XI).

In order to first quantify the prevalence of these connections in the present data, for both SEEG and MEG, we compared the estimates of CFC, PS, and AC against surrogate data to evaluate their statistical significance (see Methods XII). The proportion of significant ($p < 0.01$) CFS, PS, and AC connections from all possible connections was denoted as the connection density, *K*, and plotted with 95% confidence limits estimated by bootstrapping over the cohort. We observed inter-areal CFS in both SEEG data (Fig. 2a,b) and in MEG data (Fig. 2c,d) at small CF ratios (1:2 and 1:3) with a LF peak in the alpha (8-12 Hz, α) band, which indicates the presence of robust alpha-beta (α:β) and alpha-gamma (α:γ) CFS. In SEEG data, the LF peak was found in the range 7–12 Hz while in MEG data the peak frequency was slightly higher, in the range 8–15 Hz. We also observed α-band peaks in the corresponding frequencies in analyses of inter-areal PS (S5 Figure) and of local CFS (S6 Figure), as well as when the strength *per se* of inter-areal CFS was estimated (S7 Figure). In SEEG data, we also observed another LF peak in the δ-θ (delta-theta, 2–5 Hz) band at CFS ratios 1:2 and 1:3 indicating the presence of δ:θ and θ:α coupling. Notably, no δ-θ peak was found in PS analyses (S5 Figure). In MEG data, interestingly, we found CFS also among γ and high-γ (Hγ) bands (between LF = 30–100 Hz and HF = 60–315Hz) at ratios 1:2 and 1:3 in a number of subjects, although the wide confidence limits indicate large inter-individual variability (Figure 2c). In SEEG data, small β:Hγ and γ:Hγ peaks were found in higher ratios in individual subjects but not in group-averaged data (Figure 2a). Finally, in both MEG and SEEG, local CFS had a much greater connection density than inter-areal CFS (S6 Figure).

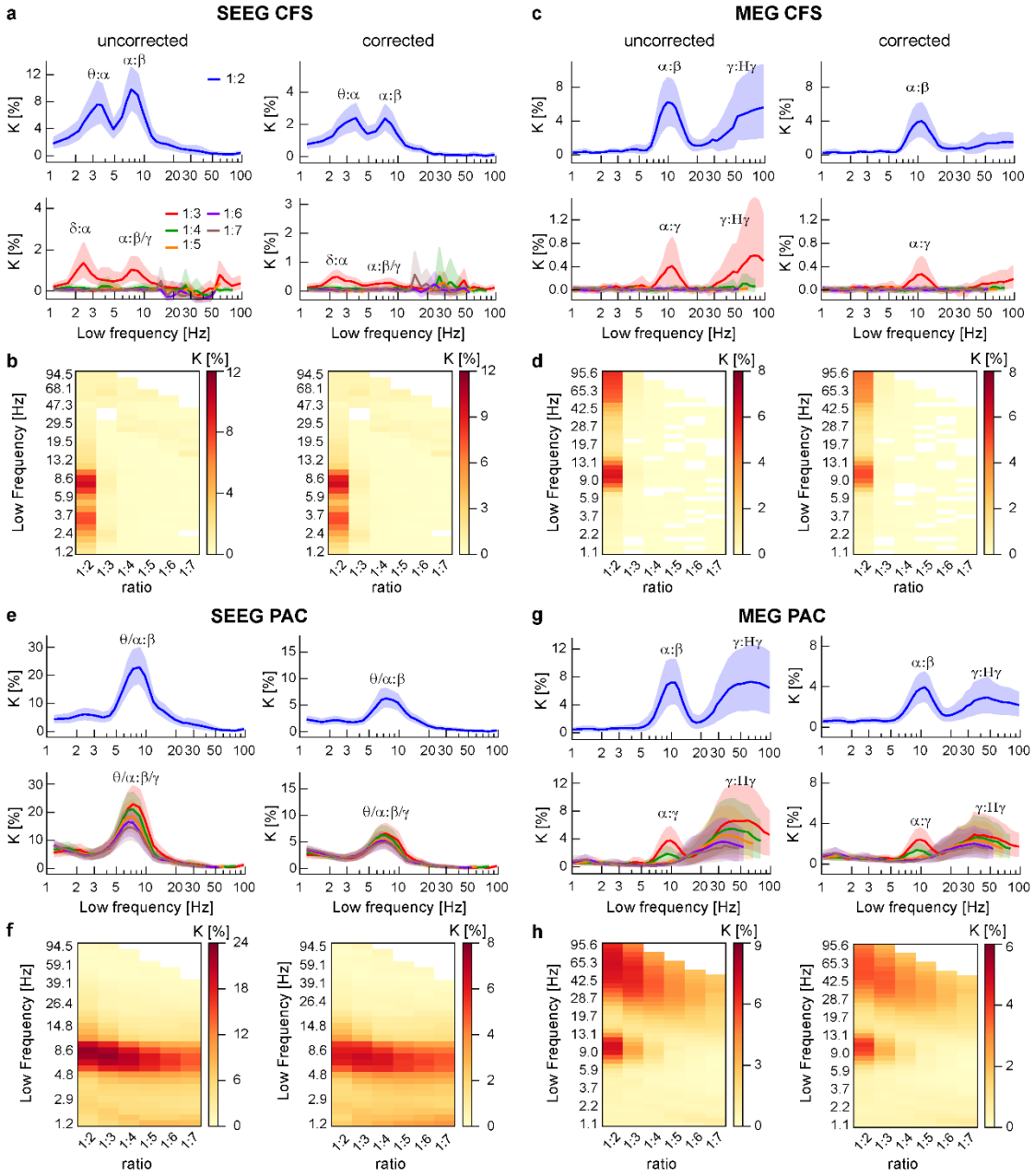

Figure 2. Inter-areal CFS and PAC are reduced but not abolished by removing spurious connections.

a) Connection density (*K*) i.e. the proportion of significant connections of all possible connections, of inter-areal CFS in SEEG data before (left) and after correcting for possible spurious connections (K_{corr}, right) for ratio 1:2 (top row) and ratios 1:2–1:7 (bottom row). The *x*-axis shows the low frequency f_1. *K* and K_{corr} are plotted with 95% confidence limits. **b)** The same data as in A), but with each frequency ratio presented as a rectangle in a matrix of the whole spectral connectome. *K* is presented before (left) and after removal of possibly spurious connections (right). **c-d)** Inter-areal CFS in MEG data before and after removing possibly spurious connections. Both in SEEG and in MEG data, *K* is reduced by removing the putatively spurious edges but 1:2 α:β and 1:3 α:γ CFS remain significantly above confidence limits. **e-f)** Inter-areal PAC in SEEG data and **g-h)** in MEG data before and after removing spurious connections. *K* for PAC is reduced by removing putatively spurious connections but remains significant for the coupling of θ-α oscillations with β–γ oscillations across ratios.

To remove all potentially spurious connections that could have been generated by only one signal, we discarded observations of inter-areal CFC between any two signals that were also connected by both inter-areal 1:1 PS (or AC for PAC) and local CFC at one or both of the locations (see Methods XIII).

After controlling for spurious connections this way, in both MEG and SEEG, the *K* values remained significantly different from zero (as indicated by the 95% confidence limits) for all observed major peaks. In MEG, the corrected *K* was a larger fraction (>50%) of the uncorrected *K* than in SEEG data (<50%). A particularly large reduction, essentially to zero-coupling levels, was observed for the γ:Hγ CFS in MEG, which suggests that this phenomenon was overall spurious, which in turn is in line with the notion of signals in this frequency range are readily contaminated by muscle artefacts (75). One possible limitation in these results so far was that for measuring 1:1 PS, we used the weighted phase lag index (wPLI) (76) that is not inflated by the linear mixing caused by signal leakage but also is insensitive to true zero-lag neuronal couplings, and may thus underestimate the true extent of PS. To eliminate this confounder, we also performed the spurious-CFC correction using the phase-locking value (PLV) as PS metric. PLV is not markedly sensitive to variation in phase difference (77) but it is inflated by linear mixing, and to account for this, we excluded the signal-leakage-dominated short-range connections from analyses of MEG data by thresholding for cross-patch PLV (see Methods VIII). Even with this limitation to medium- and long-range connectivity, we found a much greater connection density for PS measured with PLV than with wPLI in MEG (S5 Figure). Correspondingly, the correction led to a greater reduction of K in MEG CFS (S8 Figure) but, importantly, the main peaks of CFS remained significantly different from zero. In SEEG data, *K* values for PS were more similar across metrics, in line with the fact that in properly referenced SEEG, volume conduction is well controlled (7). In SEEG, the corrected *K* values for CFS obtained using PLV were very similar to those where wPLI was used (S8 Figure). Thus, regardless of the choice of the connectivity metric for PS estimation, true CFS was robust in resting-state brain activity.

We next assessed inter-areal phase-amplitude coupling (PAC) and found it highly significant in both SEEG (Fig. 2e,f) and MEG data (Fig. 2g,h). Similarly to CFS, LF peaks characterized SEEG PAC in the 5–12 Hz range and MEG PAC in the 7–15Hz range. Unlike in CFS, however, these peaks were found at all frequency ratios in SEEG data and at ratios 1:2–1:4 in MEG data. Interestingly, the peak LF in SEEG decreased with increasing ratio, although the effect was significant only before spurious CFC correction ($r = –0.91$, $p = 0.013$

for uncorrected and $r = –0.58$, $p = 0.23$ for corrected data; Pearson's correlation test on interpolated data, see Methods XIV). We also found PAC among γ and high-γ bands in MEG, as for CFS. Similarly to CFS, local PAC exhibited higher *K* values than inter-areal PAC (S6 Figure). Notably, in inter-areal PAC, we found no LF peak in the δ/θ band indicating that the observed δ/θ:α coupling in SEEG was specific to CFS. We also applied our correction method to PAC, with the notable difference that for possible triangle motifs HF interactions were estimated as correlations of amplitude envelopes, instead of PS (see Methods XIII). In SEEG, these correlations were most pronounced at very high frequencies (>200 Hz) with no preference for a specific modulation frequency (S9 Figure), at low frequencies (<10 Hz) with a preference for high modulation ratios, and at beta and low-gamma frequencies (15-40Hz) modulated by theta and low alpha frequencies (5-10Hz) of which the peak decreased similarly to LF peak in PAC ($r = -0.98$, $p < 0.001$, Pearson's test on interpolated data). Similarly trends were observable in MEG, but less pronounced, with overall larger *K* values than in SEEG. After applying the correction method, the *K* values again remained significantly above zero, this time also for the γ:Hγ PAC. Similar results were obtained using PLV as PS metric (S8 Figure). Together, these results show that true inter-areal CFS and PAC between separable sources can be observed in both SEEG and MEG data.

Inter-areal CFC is dependent on distance and cortical layer

By using a conservative approach to remove all putative false positive CFC connections, our results so far strongly supported the existence of true inter-areal CFC in resting-state brain dynamics. We next set out to investigate whether, similarly to PS, CFC was dependent on the distance between the two sources and their depth along the cortical laminae in SEEG data. We divided the electrode pairs in SEEG and parcel pairs in MEG into three distance bins containing equal numbers of connections each and computed mean 1:2 and 1:3 CFS and PAC in each of these bins (see Methods XV). In both SEEG and MEG data, CFS and PAC were observed in all distance bins (Figure 3) and the greatest PLV and K values were found for the shortest distances (blue lines) and smallest values for the longest distances (green lines) both before and after removing possibly

spurious connections (Wilcoxon test, $p < 0.05$, corrected for multiple comparisons with Benjamini-Hochberg,

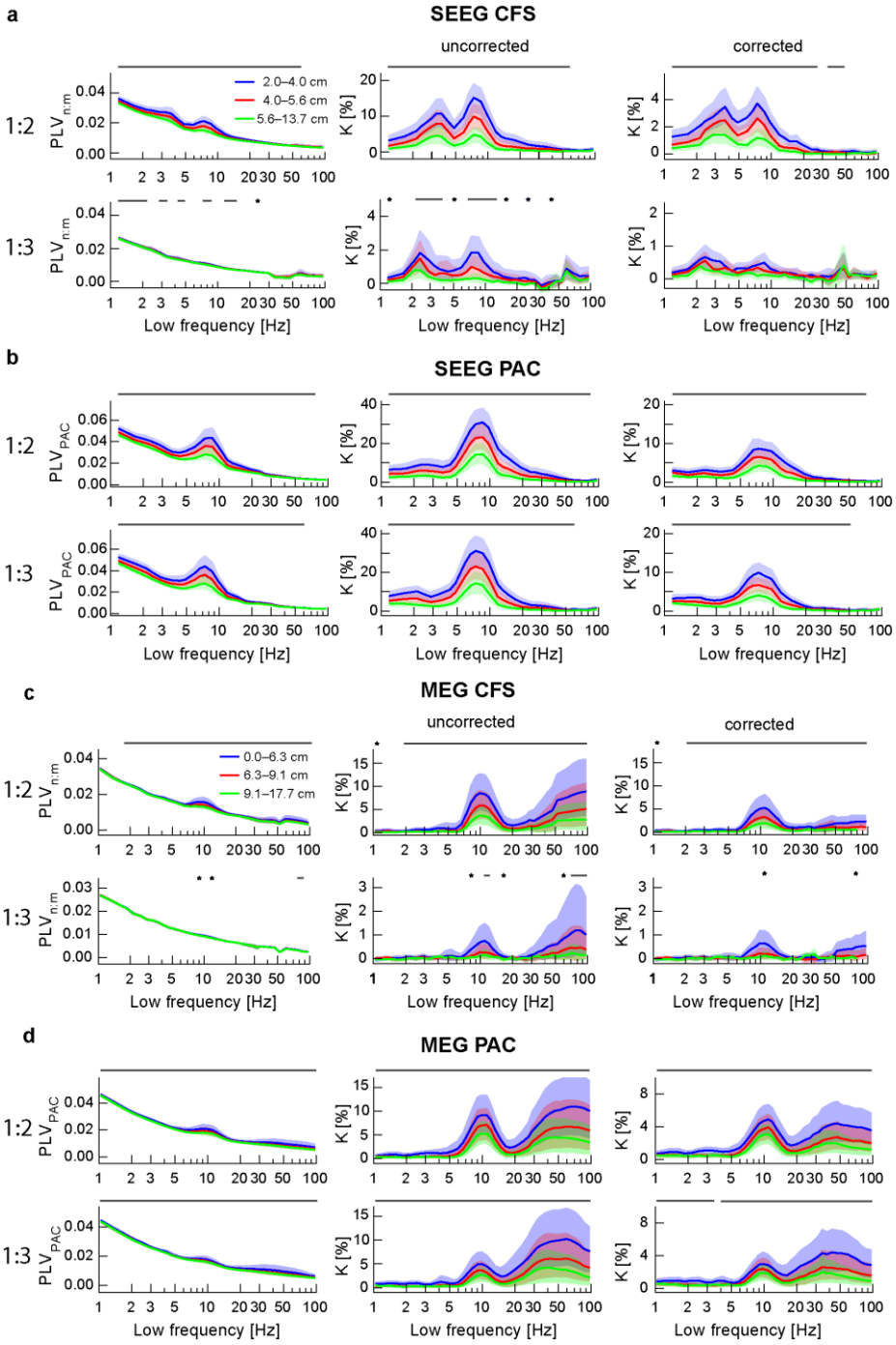

Figure 3. Inter-areal CFS and PAC decrease as a function of distance

a) Mean strength of *n*:*m* CFS (PLV, left), *K* (middle), and K_{corr} (right) of inter-areal CFS in SEEG data estimated separately in three distance bins containing equal numbers of connections for 1:2 (top row) and 1:3 (bottom row) inter-areal CFS. All values are plotted with 95% confidence limits as shades. Grey bars and stars indicate where the 1st and 3rd bin had been found to be significantly different from each other (Wilcoxon test, $p = 0.05$, corrected). **b)** Mean strength (left), *K* (middle), and K_{corr} (right) of inter-areal PAC in SEEG data in three distance bins. **c-d)** Mean strength, *K*, and K_{corr} of inter-areal CFS and PAC in MEG data. All measures, strength, *K* and K_{corr} were larger for the shortest than the longest distance bins for 1:2 CFS and for 1:2 and 1:3 PAC in both SEEG and in MEG data across most of the frequency spectrum.

exact values in S1 Table). For 1:2 CFS and 1:2 PAC, the coupling at shortest and longest distance was significantly different for almost all LFs in both uncorrected and corrected data. In 1:3 CFS, significant differences were sparser, mostly found at the main LF peaks in uncorrected data, and not present in corrected data except for two single frequencies in MEG data. In 1:3 PAC, differences were significant for LFs up to 50Hz in SEEG, and for the whole frequency range in MEG both before and after *K* correction. Similar profiles were also found for PS (S5 Figure).

We then investigated whether inter-areal 1:2 and 1:3 CFS and PAC in SEEG data would vary with the location of the electrodes in superficial or deep cortical layers (see Methods XVI), as has earlier been found for PS (7). Both CFS and PAC were more prominent between electrodes in superficial layers (red lines) than between those in deep layers (blue lines) at the main LF peaks in uncorrected data (Figure 4). Values for CFS connections between electrodes in superficial and deep layers (green and purple lines) lay between those located to either deep or superficial layers. We then tested whether CFC between electrodes both located in superficial layers was statistically significantly different from CFC between electrodes both in deep layers, which was confirmed for 1:2 CFS and both 1:2 and 1:3 PAC (Wilcoxon test, $p < 0.05$, corrected for multiple comparisons, exact values in S2 Table). After correction for possibly spurious connections however, these differences were less pronounced and not significant. In fact, in PAC, connections with the LF electrode in a deep and the HF electrode in a superficial layer were now strongest and those with the inverse relationship weakest. This difference was significant (Wilcoxon test, $p < 0.05$, corrected for multiple comparisons, exact values in S2 Table) for a number of frequencies, mainly in the θ–β range. Thus, while CFC showed a clear consistent relationship with distance between signal sources, further research is needed to clarify the localization of CFC in cortical layers and its dependence on inter-areal PS and local CFC in the correction approach.

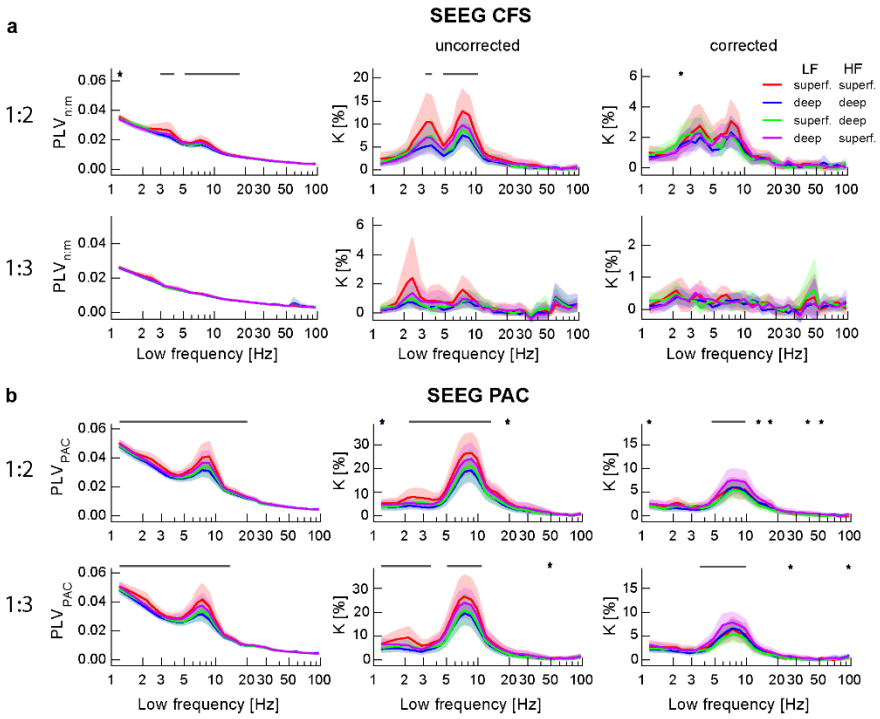

Figure 4. CFS and PAC differ between cortical layers in SEEG data

a) The mean *n*:*m* CFS strength (PLV, left), *K* (middle), and K_{corr} (right) of inter-areal 1:2 (top row) and 1:3 (bottom row) CFS in SEEG data. CFS connections are shown among electrode pairs that were either both in superficial layers (red), both in deep layers (blue), where the low-frequency (LF, f_1) electrode was in a superficial layer and the high-frequency (HF, f_2) electrode in a deep layer (green) and where LF electrode was in a deep layer and HF electrode in a superficial layer (purple). Grey bars and stars indicate where the strongest and weakest values (red and blue in left and middle column and purple and green in right column were significantly different (Wilcoxon test, $p = 0.05$, corrected) in consecutive or single frequencies. **b)** The same as in (a) for the inter-areal PAC in SEEG data. In both CFS and PAC, strength and *K* are stronger for connections which are within superficial than within deep layers while the CFS and PAC between deep and superficial layers have intermediate strengths.

Low- and high-frequency hubs differ between CFS and PAC

Lastly, we identified the anatomical-topological architectures of CFS and PAC connectomes. We first used a conventional in- and out-degree-based graph theoretical approach (78) to estimate LF and HF "hubness" (see Methods XVII). We estimated, for each frequency pair of the main peaks, for each of the 148 parcels, the relative directed degree as a measure of whether the parcel was predominantly a HF or LF hub. For CFS networks, in both SEEG and MEG data, for 1:2 α:β and 1:3 α:γ CFS, HF hubs (red) were observed in somatomotor (SM) regions, posterior parietal cortex (PPC), and temporal cortex (Figure 5). LF hubs (blue) were localized to regions lateral prefrontal cortex (lPFC) and medial parietal cortex (MPC) in both SEEG and MEG, that belong to default mode, control and salience networks in the functional parcellation (see S10 Figure)

based on fMRI BOLD signal fluctuations (79) and also in occipital cortex in 1:2 α:β in MEG. However, for PAC, we observed the opposite localization of LF and HF hubs in most cortical regions except the occipital pole. We found the LF hubs for 1:2 α:β and 1:3 α:γ PAC to be consistently localized in SM, PPC and occipito-temporal regions in both SEEG and MEG, and the HF hubs mainly localized in frontal regions and MPC. In 1:2 θ:α and 1:3 δ:α CFS, which were specific to SEEG, patterns were similar to 1:2 α:β and 1:3 α:γ CFS. In order to confirm the similarity between SEEG and MEG data and the dissimilarity between CFS and PAC, we computed the correlation of relative directed degree values across parcels using Spearman's test. A significant ($p < 0.05$) positive correlation between SEEG and MEG was found for PAC, and a non-significant one for 1:2 CFS (Table 1). We found values for CFS and PAC to be significantly anti-correlated ($p < 0.05$) for 1:2 and 1:3 SEEG and 1:2 MEG, and non-significantly anti-correlated for 1:3 MEG (Table 2).

Secondly, we estimated the directionality of CFC connections between parcels, i.e. if some parcels would be involved in CFC connections as predominantly the site of either the LF or HF oscillation. We estimated the low-vs.-high directionality for each parcel pair and each frequency pair of the main peaks across subjects (see Methods XVIII). Significant directionality between the two parcels was established if the absolute value of directionality was higher than in 95% of permutations. We then averaged for each parcel the significant directionality values, again yielding a positive value for parcels that can be interpreted as HF hubs and a negative value for parcels that can be interpreted as LF hubs. Results were remarkably similar to those of the degree-based hubness analysis, showing the same dissociation between CFS and PAC (Figure 6). Taken together, these results provide strong evidence that the anatomy and structure of CFS and PAC connectomes are distinct, demonstrating the presence of two different forms of CFC RSNs with particular directional patterns. Again, we computed the similarity between SEEG and MEG and dissimilarity between CFS and PAC using the Spearman's test, yielding similar results as for directed degree (Tables 1,2).

Table 1: Parcel values are correlated between SEEG and MEG data

	Rel. dir. degree		Directionality	
	r	**p**	**r**	**p**
1:2 CFS	0.136	0.101	0.094	0.254
1:2 PAC	**0.233**	**0.004**	**0.259**	**0.002**
1:3 CFS	-0.052	0.531	0.130	0.114
1:3 PAC	**0.203**	**0.013**	**0.314**	**$<10^{-4}$**

Values obtained with Spearman's test. Significant correlations ($p < 0.05$) in bold.

Table 2: Parcel values are anticorrelated between CFS and PAC

	Rel. dir. degree		Directionality	
	r	**p**	**r**	**p**
1:2 SEEG	**-0.254**	**0.002**	**-0.277**	**0.001**
1:2 MEG	-0.114	0.168	-0.106	0.200
1:3 SEEG	**-0.241**	**0.003**	0.018	0.831
1:3 MEG	**-0.240**	**0.003**	**-0.252**	**0.002**

Values obtained with Spearman's test. Significant correlations ($p < 0.05$) in bold.

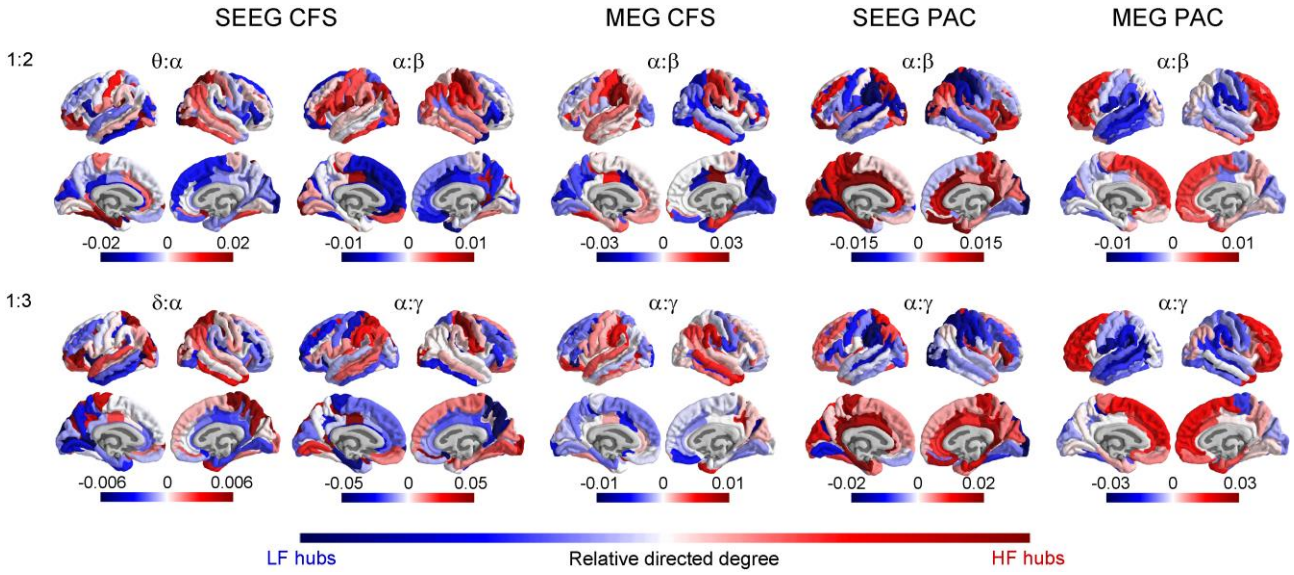

Figure 5. CFC networks have an asymmetric low- and high-frequency hub architecture

Relative low (f_1) vs. high (f_2) degree of each brain region (parcel) for CFS and PAC networks. Relative degree values indicate whether parcel is primarily a hub for the low frequency (f_1, red) or high frequency (f_2, blue) in inter-areal CFC. Top row: Brain anatomy of CFS and PAC at ratio 1:2 connecting θ:α and α:β frequencies. Bottom row: Brain anatomy of CFS and PAC networks at ratio 1:3 connecting δ:α and α:γ frequencies. CFS and PAC networks show saliently opposing anatomical structures connecting anterior and posterior brain regions.

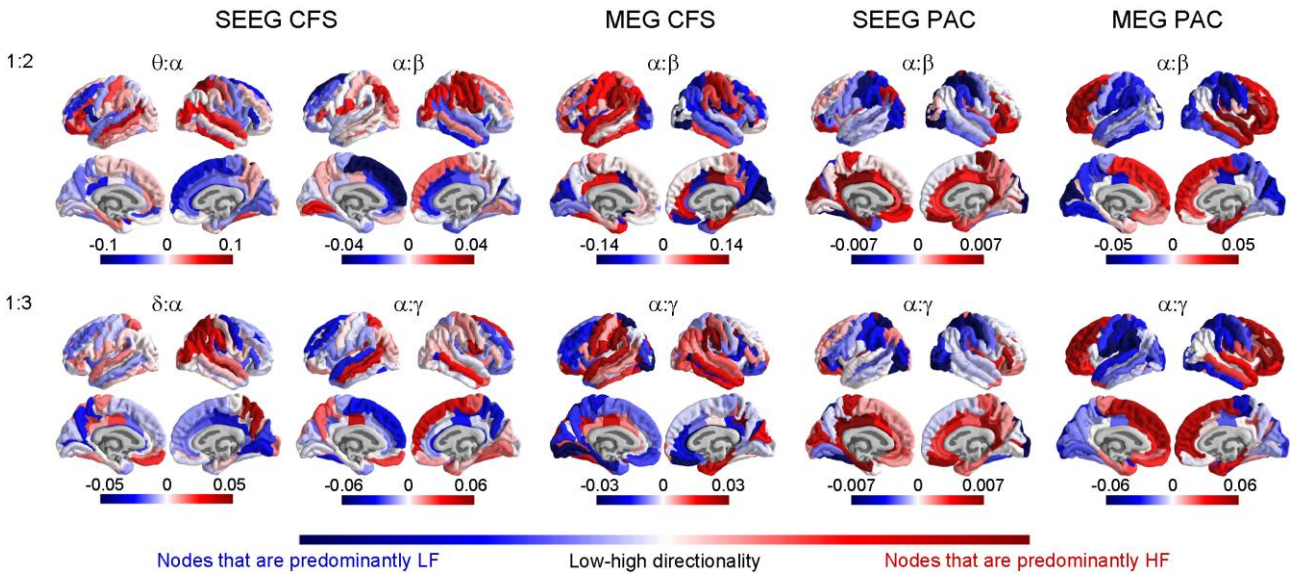

Figure 6. Asymmetric directional connectivity in CFC networks

Averaged low (f_1) vs. high (f_2) -directionality values for each parcel. The values indicate whether parcel is a directional hub for f_1 (red) or for f_2 (blue) in inter-areal CFC networks. Top row: Directionality for CFS and PAC networks at ratio 1:2 connecting θ:α and α:β frequencies. Bottom row: Directionality for CFS and PAC at ratio 1:3 connecting δ:α and α:γ frequencies. Directional connections of CFS and PAC networks reflect their structure in brain anatomy and show similar opposite directional connections connecting anterior and posterior brain regions as seen in degree hub analysis.

Discussion

Human brain activity during rest, as revealed originally by fMRI, is characterized by intrinsically correlated fluctuations among constellations of brain regions, known as RSNs (16,80,81). Also in human electrophysiological measurements, PS and amplitude correlations of neuronal oscillations characterize resting-state activity in a wide range of frequencies in anatomically well delineated and modular structures (82). In this study, we have used a novel approach to investigate two forms of large-scale neuronal cross-frequency coupling (CFC) in human resting state activity. We identified the networks that connected neuronal oscillations of different frequencies across brain regions with both SEEG and MEG data by using a novel method for dissecting true from potentially spurious observations of CFC. We found that two distinct types of true CFC, cross-frequency synchrony (CFS) and phase-amplitude coupling (PAC), to characterize human resting-state activity. CFS and PAC networks showed distinct spectral profiles, anatomical architectures, and coupling directions among brain regions.

Large-scale CFC networks characterize human resting state activity

A number of studies have previously reported local PAC (27-29,33,34,56-58,65,83) and CFS (4,8,36,37,59-61) in human M/EEG and intracranial data. Both PAC (26,40-42,42,45-47) and CFS (4,43,47,48) have been proposed to be central mechanisms for coordinating spectrally distributed neuronal processing and thereby regulating the communication in multi-scale oscillatory networks. Despite extensive research, only few prior studies have also examined inter-areal CFC (4,36,39,63,64). One study has found initial evidence for the presence of PAC networks between theta and gamma oscillations, but not between other frequencies, during resting state activity (64) and the resting-state connectomes of CFS have not been charted in any of the prior studies save for a MEG-sensor-level analysis (4).

We found both inter-areal PAC and CFS to characterize both MEG and SEEG data during RS activity. Robust increases in local α oscillations have been known to be a marker of resting human brain for several decades (20,84-87). Here we show that α oscillations are also cross-frequency coupled with the faster β and γ frequency oscillations in both MEG and SEEG data. These CFC couplings were similar to those observed in task states

(4,39), which is in line with suggestions of RSNs forming the underlying core of task-state networks (88). The presence of both PAC and CFS during human RS indicates that the phase of α oscillations both couples with the amplitude of β and γ oscillations through PAC and is also aligned with β and γ oscillation phases via CFS spontaneously during intrinsic activity fluctuations.

Inter-areal CFS connected θ/α oscillations with β and γ oscillations only at small frequency ratios of 1:2 and 1:3, while PAC of θ and α oscillations with higher frequencies was robust throughout ratios from 1:2 up to 1:7 in SEEG data and up to 1:4 in MEG data. Hence, in contrast to CFS, PAC in the θ and α bands were found also at high ratios in SEEG data, demonstrating that excitability fluctuations reflected in slow oscillations are coupled to the strength of fast oscillations over a wide frequency range, either through slow modulation of fast activity or as the temporally summed postsynaptic impact of intermittent fast activity per se. This is in line with the previous findings of θ:γ PAC at high ratios in the rat hippocampus (49,51-53) and in human intracranial recordings (27,28,34,38,65). The lack of high frequency ratios in CFS is not surprising as in CFS, stable phase-difference between coupled oscillations is associated with consistent spike-time relationships between the neuronal assemblies in different frequency bands and these are unlikely to be present over wide frequency ratios due to the conceivably limited temporal accuracy in the mechanisms of the slower oscillation. Although in MEG and EEG data resting-state activity usually peaks at α frequencies, this peak is typically lower in epileptic patients (89). Accordingly, we found the main α peak in SEEG to be observable at around 7-8 Hz. Interestingly, in SEEG data, also δ–θ oscillations were coupled with α band oscillations by CFS. Crucially, no peak in within-frequency PS or in PAC was observed in the δ–θ band, indicating that δ/θ:α coupling was a CFS-specific phenomenon.

Characteristics of CFC networks in the resting human brain

Central unresolved questions are whether CFC RSNs can be observed in the resting human brain activity with consistent large-scale architectures and whether they exhibit characteristics are similar to those observed in within-frequency coupled RSNs. Prior studies have found 1:1 PS in SEEG (7) and in MEG data (4,14,82,90) to decrease as a function of distance. In this study, we found salient inter-areal CFC to characterize resting-

state brain activity so that the connection density of CFS and PAC decreased with distance between cortical parcels (MEG) or electrode contacts (SEEG) similarly to that of inter-areal PS, which is in line with previous results of CFS in MEG sensor space data (4).

Intracortical recordings have shown that oscillations of different frequencies are generated differentially across cortical layers (91-94). Here we identified the cortical depth of each SEEG electrode (7,95) and found that before the exclusion of potentially spurious connections, α:β CFS as well as δ:α, θ:α/β and α:β/γ PAC were significantly stronger among electrode pairs that were both located in superficial layers than between pairs both located in deep layers. However, in corrected PAC data, we found the largest connection density values for connections where the slow oscillation was located in the deep layers and the fast oscillation in the superficial layers, and conversely the lowest values for those where it was vice-versa. These findings are in line with previous results that reported γ synchrony to be strongest in superficial layers, whereas α synchrony was found in deep and superficial layers (92,93,96). One should however note that due to lack of current source density analyses, for which the SEEG electrode-contact separation is too large, and because of complex current source geometries in cortical circuitry and the volume conduction between layers (93), further studies are required to investigate the localization of CFC in different cortical layers.

Distinct large-scale organization of CFS and PAC RSNs

To assess the large-scale architecture of the cortical CFC networks, we used two strategies for identifying LF and HF hubs, *i.e.*, brain regions where predominantly the slower or the faster oscillations of the CFC connection are observed. Both approaches converged on showing robust anatomical asymmetries in LF and HF hubs of α:β, α:γ and δ/θ:α inter-areal CFC. In both SEEG and MEG, CFC RSNs coupled anterior and posterior brain regions. The localization of hubs was similar between SEEG and MEG data, which corroborates the validity of our findings. Importantly, however, we observed distinct and partially opposing localization of the LF/HF hubs for CFS and PAC. In α:β and α:γ CFS, the α LF hubs were observed in PFC and medial regions that belong to the default mode network (16,81) or to control and salience networks in the functional parcellation based on fMRI BOLD signal fluctuations (18,79,97). Many previous studies have found α oscillations in these regions to be correlated with attentional and executive functions (20,23,24,87,98). In

contrast, the β and γ HF hubs were found in more posterior regions such as sensorimotor region (SM) and the occipital and temporal cortices where β and γ oscillations are often associated with sensory processing (99-102).

In contrast to CFS, the α LF hubs of α:β and α:γ PAC were found in occipital, temporal, and posterior parietal cortex whereas the β and γ HF hubs in prefrontal and medial parietal cortex, which was essentially opposite to the anatomical structure observed for CFS. Hence, both CFS and PAC RSNs coordinated cross-frequency coupling of oscillations along the anterior-posterior, or higher-to-lower-order, brain systems, which suggests that they reflect the network interactions for the coordination among attentional and executive networks and task-positive sensory networks. In addition, the spectral differences and distinct large-scale structures of CFS and PAC demonstrate that CFS and PAC are separable computational and neurophysiological mechanisms rather than operationalizations of a hypothetical shared underlying "CFC" construct. This conclusion is in line with prior findings during task performance (39). The localization of CFS and PAC showed that both are, nevertheless, likely to coordinate intrinsic interactions among attention, control and default-mode networks on the one hand and sensory processing systems on the other, and therefore are likely to regulate the interactions between intrinsic and extrinsic processing. Overall, our data extends the scarce previous findings of inter-areal θ:α, α:β and α:γ CFS and θ:α–γ PAC observed earlier in source-reconstructed MEG/EEG data during VWM (39) in fronto-parietal and visual systems, and of inter-areal θ:γ CFS between hippocampus and prefrontal cortex in human intracranial EEG data (38).

True positive inter-areal CFC not explained by spurious connections characterize resting state activity

Multiple concerns have been raised about the validity of previous observations of CFC (66,67,69-72,103). A common point of critique is that non-sinusoidal waveforms or linear fast components (67) lead to observations of spurious CFC by causing higher-frequency filtering artefacts that are locked to the waveform. Although most of these critiques relate to PAC (66,103), and critique is raised mostly against local CFC (70,72), the confounding effects of non-sinusoidal waveforms apply to CFS as well and may also lead to spurious inter-

areal CFC through a combination of local CFC and inter-areal within-frequency coupling. Furthermore, another family of possible confounders is posed by amplitude fluctuations of oscillations or activities with a non-zero mean (73), which lead to spurious observations of lower-frequency oscillations by filtering and thereby to spurious observations of CFC or PAC in particular.

In this study, we mapped human CFC RSNs from SEEG and source-reconstructed MEG data. To identify true neuronal CFC from amongst the spurious connections, we took advantage of the fact that inter-areal CFC can only be spurious when the two signals are connected also via within-frequency (1:1) PS, or amplitude correlations in the case of PAC, and local CFC. Thus, if this is not the case, the two signals can be assumed to be from separable processes and an observation of inter-areal CFC between these signals are true. We used this rationale in a novel graph-based analytical approach to control for possibly spurious CFC connections by discarding those CFC observations between two signals that were also connected by inter-areal 1:1 phase synchronization (PS) of oscillations or of their amplitude envelopes (for the high frequency in PAC) and local CFC. Since this approach also may discard some true instances of inter-areal CFC, it gives a conservative estimate of the presence of true neuronal inter-areal CFC. We used this approach to show that true neuronal CFC characterizes human brain activity in both MEG and SEEG datasets. Our results demonstrate that true neuronal CFC characterizes human resting state activity and couples θ and α oscillations with faster oscillations in the β- and γ-frequency bands. The number of significant connections was reduced by exclusion of the potentially spurious corrections, indicating that part of the commonly observed CFC in MEEG and SEEG data may indeed be caused by higher-frequency filter artefacts arising from non-sinusoidal signal components (66,67,69-72), or by amplitude fluctuations of non-zero-mean waveforms (73). However, our results clearly indicate that in addition to possibly spurious CFC, also true neuronal CFC that cannot be explained by such artefacts is observable in MEG and SEEG data.

We observed also local CFS and PAC to showed similar spectral distributions to inter-areal CFS and PAC, respectively but with a greater fraction of significant observations. However, for local CFS and PAC, there is no way to unequivocally distinguish between true and artefactual observations and hence the functional significance of local CFC remains an open question. Moderately divergent findings between SEEG and MEG may partially be explained by larger source-mixing in MEG, but also are in line with the fact that MEG and SEEG are partially sensitive to distinct aspects of neuronal processes.

Methodological considerations

We used in this study a novel approach to identify true inter-areal CFC and discard putatively spurious connections by evaluating in multi-site recording data whether there is evidence for separable neuronal oscillations. Given the accuracy of SEEG data and the fact that findings were similar between SEEG and MEG, our observations establish the presence of true neuronal CFC to be a prominent feature of human resting state electrophysiological activity. True neuronal CFC, by definition, is a coupling between two separate neuronal processes while spurious CFC can be caused by filter artefacts in higher harmonic frequencies of a non-sinusoidal process, or by filter artefacts in lower frequencies stemming from amplitude fluctuations of non-zero-mean oscillations. We hence removed inter-areal CFC observations between oscillations that were also be connected by local CFC and PS and thus could not be safely assumed to be independent processes. The number of removed connections hence depends on the connection density of PS, which will differ between different metrics of PS. In MEG, observation of artificial connections in PS can arise due to volume conduction when using metrics such as the phase-locking value (PLV) (44,77,104). Artificial PS from volume conduction has zero phase lag and can be avoided using the weighted Phase-Lag Index, wPLI (76) that is insensitive to near-zero-lag connections. Therefore, the wPLI is much less likely to report false positives, but also discards actual connections with zero phase lag, and can thus lead to some false negatives. In MEG data, PS was indeed higher when using PLV than wPLI which led to a larger reduction of CFS in MEG during correction, nevertheless, the connection density of corrected CFS and PAC still remained significantly different from zero. In SEEG data, where there the effect of volume conduction is negligible with proper referencing, there were no major differences in PS between the two metrics and the true CFS estimated with these approaches were similar. These complementing results further strengthen the evidence for the presence of true inter-areal CFC.

Conclusions

We show here that large-scale networks of true neuronal CFS and PAC characterize human resting-state brain activity in SEEG and in MEG data. Using a new graph theoretic approach, we validated that the observations

of CFC were not explainable by filter artefacts. The CFC RSNs were akin both to known RSNs of phase synchrony and fMRI BOLD correlations. CFC RSNs had a large-scale structure connecting slow and fast oscillations between anterior and posterior parts of the brain. Salient differences in brain anatomy and spectral properties demonstrated CFS and PAC RSNs were distinct and can be assumed to serve different computational functions. Altogether, converging results from meso- and macroscale electrophysiological recordings and two different populations provide strong evidence for the existence of two forms of true neuronal CFC during human resting state and reveal their large-scale network organization.

Data and code availability statement

The connectomes underlying all results presented in Figures 2-6 and S3-S9 are available on DataDryad (https://datadryad.org/review?doi=doi:10.5061/dryad.0k86k80). These files contain pairwise inter-areal CFC and PS interactions between all parcels or electrode contacts, and local CFC interactions, for each subject. Also included are support files containing such information as filtering parameters, cortical parcellations, location of electrode contacts. Raw data cannot be made available due to data privacy regulations set by the ethical committee. All quantitative results presented in the manuscript are based on this data. The code used to obtain these results can be found on GitHub (https://github.com/palvalab/Resting_State_CFC).

Acknowledgements:

We thank Salla Markkinen, Santeri Rouhinen, Jaana Simola, Jonni Hirvonen and Sami Karadeniz for the help in MEG recordings and Annalisa Rubino for the help in SEEG recordings.

Funding Disclosure

This work was supported by the Academy of Finland (SA 266402 and 1303933 to SP and SA 253130 and 256472 MP).

Competing interests

The authors declare no competing interests.

Methods

I. SEEG Data acquisition

Stereo-electroencephalography (SEEG) data were recorded from 59 subjects affected by drug resistant focal epilepsy undergoing pre-surgical clinical assessment at "Claudio Munari" Epilepsy Surgery Centre, Niguarda Hospital, Milan. "Monopolar", i.e. bipolar with a single shared reference in the white matter, local field potentials (LFPs) were recorded from brain tissue with platinum–iridium, multi-lead electrodes with 8-15 contacts each. These contacts were 2 mm long, 0.8 mm thick, and had an inter-contact border-to-border distance of 1.5 mm (DIXI medical, Besancon, France). Anatomical positions and numbers of electrodes varied according to surgical requirements (105).

From each subject, one 10-minute set of eyes-closed resting state data was recorded with a 192-channel SEEG amplifier system (NIHON-KOHDEN NEUROFAX-110) at a sampling rate of 1000 Hz. Electrode positions were assessed with computer-tomographic (CT) scans after implantation using the SEEGA tool (106). Structural MRIs were also recorded prior to the electrode insertion and a rigid-body coregistration was used to co-localize MRIs and post-implant CT scans (105). Based on this, electrode contacts were assigned to one of 148 parcels of the Destrieux atlas (74).

Subjects gave written informed consent for participation in research studies. The recording of this data was approved by the ethical committee (ID 939) of the Niguarda "Ca' Granda" Hospital, Milan, and was performed according to the Declaration of Helsinki.

II. SEEG Data preprocessing and filtering

Defective electrode contacts were identified by clearly non–physiological activity and excluded from analysis. For referencing, we used the closest-white matter referencing scheme (95) where each contact in cortical grey matter is referenced to the nearest contact in white matter. The seizure onset and propagation zone were identified by clinical experts in visual analysis and contacts in these areas were excluded from analysis, as were contacts from subcortical regions. We excluded from connectivity analyses those contact pairs that shared

the same reference or had a contact-to-contact distance < 2 cm in order to avoid spurious connectivity due to volume conduction.

Due to possible filtering artefacts around epileptic spikes, periods of 500 ms duration containing Interictal Epileptic (IIE) events were discarded, where at least 10% of contacts in narrow-band time series demonstrated abnormal concurrent sharp peaks in more than half of frequency bands. To identify such periods, we first searched for "spiky" periods in amplitude envelops for each contact with 500 ms non-overlapping time windows along the whole recording. A 500 ms time window was tagged as "spiky" when any of its samples was greater than the contact mean amplitude plus 5 times the contact's standard deviation. Band-stop filters were applied at 50 Hz and 100 Hz to filter out line noise. Time series were then filtered with Morlet wavelets with $m = 5$ (107) using 49 center frequencies from 1.2 to 315 Hz.

III. MEG and MRI Data acquisition

306 channel MEG (204 planar gradiometers and 102 magnetometers) was recorded with a Vectorview-Triux (Elekta-Neuromag) at the BioMag Laboratory, HUS Medical Imaging Center from 19 healthy participants during 10 minutes eyes-open resting state session. Overall 27 sets of resting state MEG data were obtained, with 4 participants contributing 2 sets and 2 participants contributing 3 sets. Subjects were instructed to focus on a cross on the screen in front of them. EOG (horizontal and vertical channels) were recorded for the detection of ocular artefacts. MEG and EOG were recorded at 1000 Hz sampling rate. T1-weighted anatomical MRI scans were obtained for cortical surface reconstruction models at a resolution of 1x1x1 mm with a 1.5 T MRI scanner (Siemens, Germany) at Helsinki University Central Hospital. This study was approved by the ethical committee of Helsinki University Central hospital and was performed according to the Declaration of Helsinki. Written informed consent was obtained from each subject prior to the experiment.

IV. MEG data preprocessing and filtering Maxfilter with temporal signal space separation (tSSS) (108) (Elekta Neuromag Ltd., Finland) was used to suppress extra-cranial noise from MEG sensors and to interpolate bad channels. Using independent component analysis (ICA, Matlab toolbox Fieldtrip, http://fieldtrip.fcdonders.nl, (109)) we extracted and identified components that were correlated with ocular artefacts (identified using the EOG signal), heart-beat artefacts (identified using the magnetometer signal as a reference) or muscle artefacts. Time series data were then filtered into narrow-band time series using a bank

of 53 Morlet filters with m = 5 and approximately log-linearly spaced center frequencies ranging from 1.1 to 315 Hz. The time-series data were down-sampled after filtering to a sampling rate approx. 5 times the center frequency to minimize data size.

V. MEG source reconstruction: preparation of forward and inverse operators

FreeSurfer software (http://surfer.nmr.mgh.harvard.edu/) was used for volumetric segmentation of MRI data, flattening, cortical parcellation, and neuroanatomical labeling with the Destrieux atlas. ((74,110,111). We obtained a cortical parcellation of 200 parcels by iteratively splitting the largest parcels of the Destrieux atlas along their most elongated axis at the group-level (10,100,112). All analyses were carried out using this parcellation, except the directionality analysis (see below), for which the data were collapsed back to the 148-parcel Destrieux atlas to facilitate the comparison with SEEG data. MNE software (http://martinos.org/mne/stable/index.html) (113,114) was used to create cortically constrained source models, a MEG-MRI co-localization and for the preparation of the forward and inverse operators. The source models had dipole orientations fixed to pial surface normals and a 5 mm inter-dipole separation throughout the cortex, yielding 5086–7857 source vertices per hemisphere.

VI. MEG source reconstruction: inverse transform

We computed Noise Covariance Matrices (NCMs) using preprocessed broadband filtered (151-249 Hz) MEG resting-state data time series, evaluated in 60 time windows of 10 s. The frequency band used for creating NCMs comprises environmental, sensor, and biological noise components, but less neuronal activity than the lower frequency bands. These NCMs were then used for creating inverse operators. A single inverse operator created as described above was used for all wavelet frequencies. To reconstruct ongoing cortical phase-time series, the filtered single-trial MEG time-series were inverse transformed.

VII. MEG Source collapsing

The source-vertex narrowband complex time-series were then collapsed into cortical parcel time-series in 200 of the split Destrieux atlas. To obtain optimal source-reconstruction accuracy, single source vertex time series were collapsed into parcel time series after weighting with fidelity-optimized collapse operator (112). Using

the neuroanatomical parcellation as a coordinate system allows the inter-subject representation of the MEG data for the group level analysis without morphing the data from individual subjects.

VIII. Removal of low-fidelity parcels from MEG connectivity analysis

In phase-synchrony analyses of parcel time-series data, one of the major confounding factors is spurious edges resulting from signal mixing between neighboring brain regions in data-acquisition and source-reconstruction (44,104). We assessed the reliability of data based on phase-correlations between real and simulated data. We estimated *parcel fidelity*, the phase correlation between the original simulated true parcel and the corresponding forward-andinverse modelled parcel time series, for all 200 parcels and *cross-patch mixing*, phase correlation between the original simulated true parcel and the corresponding forward-and-inverse modelled parcel time series of all other parcels, for all parcel pairs (112). To decrease the probability of spurious synchronization, for wPLI analysis, we excluded parcels with a fidelity <0.1, retaining 187 of parcels and 34782 or 87.4% of connections. For PLV analysis, which is affected by signal mixing, we additionally excluded parcel pairs with cross-patch PLV > 0.2143, which are thought to be affected strongly by mixing, so that in these analyses we retained 28416 or 71.4% of connections. This threshold for cross-patch PLV was obtained as 1.95 times the mean value in the simulations, which roughly corresponds to $p < 0.05$ significance level. The removed parcels and connections were located mostly to deep and / or inferior sources, which generate the least detectable signals in MEG and which are hence most likely to generate spurious connections.

IX. Analysis of inter-areal phase-synchronization (PS)

To identify cortex-wide phase-synchrony (PS) networks, we first computed individual parcel-to-parcel (MEG data) or contact-contact (SEEG data) interaction matrices. Phase synchrony (PS) was estimated using the weighted phase-lag index (wPLI) (76) as well as the phase-locking value (PLV) (4,35). Because of source leakage, the use of PLV leads to the detection of zero-phase lag artificial interactions, while wPLI is insensitive to zero-phase lag interactions and hence less affected by artificial interactions (44,115).

We computed PS across the whole time series for each frequency, and each contact pair or parcel pair *i, j* as:

$$wPLI_{i,j} = \frac{|E\{im(X_{ij})\}|}{E\{|im(X_{ij})|\}} \quad (1)$$

, where $im(X_{ij})$ is the imaginary part of the cross-spectrum of the complex time series Z_i and Z_j, and $E\{\ \}$ is the expectancy value operator, and:

$$PLV_{i,j} = \frac{1}{N}\left|\sum_t \exp\{i(\theta_i - \theta_j)\}\right| \quad (2)$$

where θ is the phase of the complex filtered time series Z and N the number of samples t. We also calculated for each contact or parcel pair one surrogate PS value where Z_j had been time-shifted by a random number of samples between 0 and N. For wPLI, we rejected connections with a z-score below 2, corresponding to α level 0.01. The PLV of uncorrelated and uniformly distributed phases can be described by the Rayleigh distribution. We used the Rayleigh distribution to estimate a confidence limit of 2.42 for the ratio of PS_{meas}/PS_{surr} at α level 0.01 (4), where PS_{meas} is the measured value and PS_{surr} is the mean over the surrogate values from all valid contact pairs or parcel pairs. Connections for which that ratio exceeded 2.42 were deemed significant.

X. Analysis of local and inter-areal of cross-frequency coupling (CFC): PAC and CFS

CFS and PAC were computed between all low-frequency (LF) at f_1 and high-frequency (HF) at f_2 combinations for each frequency ratio 1:m from 1:2 to 1:7 and for each contact -pair i,j in SEEG data and for each parcel-pair i,j in MEG data. CFS was computed as:

$$PLV_{i,j,m} = \frac{1}{N}\left|\sum_t \exp\left[\mathrm{i}\cdot\left(m\cdot\theta_{i,LF} - \theta_{j,HF}\right)\right]\right| \quad (3)$$

where $\theta_{i,LF}$ and $\theta_{j,HF}$ are the phases of the time series of contact /parcels i,j and $\theta_{i,LF}$ has been upsampled to match the sampling rate of the HF signal (4,39). Local CFS (CFS_{loc}) was obtained where $i=j$, inter-areal CFS where $i\neq j$.

PAC was computed as:

$$PAC_{i,j,m} = \frac{1}{N}\left|\sum_t \exp\left[\mathrm{i}\cdot\left(\theta_{i,LF} - \theta_j^{env}\right)\right]\right| \quad (4)$$

, where $\theta^{env}_{j,HF,LF}$ is the phase of the amplitude envelope of the HF signal filtered with a Morlet filter at LF, and downsampled to match the LF signal's sampling rate. Local PAC was obtained where $i=j$, inter-areal PAC where $i \neq j$ (25).

XI. Analysis of amplitude-amplitude coupling

To estimate within-frequency amplitude correlations (AC), and as a pre-requisite to removal of potentially spurious PAC (see next section), we also computed pairwise phase correlations of LF-modulated amplitude envelopes of the HF signals. This was done by computing within-frequency phase synchrony between the phases of the LF-filtered amplitude envelopes $\theta^{env}_{j,HF,LF}$ for all contact pairs or parcel pairs $i \neq j$ using all frequency pairs LF, HF that were used for PAC computations.

XII. Group-level statistics

For the group-level statistics of PS, AC, CFS, PAC, CFS_{local} and PAC_{local}, we computed upper and lower confidence limits (2.5% and 97.5%) with bootstrapping approach using $N = 1000$. We pooled significant edges across subjects to obtain the mean strength and the group-level connection density over all channels (in SEEG) or parcels (MEG). Since it can be expected that in the absence of any true interactions, 1% of edges would be reported as significant anyways as statistical false positives, we subtracted 0.01 from all reported/plotted K values.

XIII. Removal of potentially spurious CFC connections

The core tenet of CFC is that it indicates an interaction between two distinct neuronal processes and hence CFC is true when there is evidence for the presence of two separate signals. Conversely, CFC may be spurious if evidence of the presence of two separate signals is not obtained and it remains a possibility that a single leaked non-sinusoidal signal or two inter-areally *within-frequency* coupled, non-sinusoidal signals may account for the observation of inter-areal *cross-frequency* coupling. We developed a conservative connection-by-connection test of whether inter-areal CFC can unambiguously be attributed to two separable signals. In this test, observations of inter-areal CFC are discarded between any two such signals that are also connected by both inter-areal 1:1 PS/AC and local CFC at one or both of the locations. In effect, this implies that all inter-areal CFC connections are removed that are observed with one of the triangle motifs shown in Figure 1f for

spurious inter-areal CFC (right panel) or for true inter-areal CFC that was ambiguous (middle panel). Whether 1:1 PS or AC is used depends on the form of CFC so that inter-areal CFS was removed when there was a triangle motif of local CFS at the parcel/contact of the low frequency (LF) oscillation and high-frequency (HF) PS between the parcels/contacts or vice versa when there was local CFS at the parcel/contact of the HF oscillation and low-frequency PS between the parcels/contacts.

Inter-areal PAC was removed when there was a triangle motif of either local PAC at the parcel/contact of the HF oscillation and low-frequency PS between the parcels/contacts or vice versa when there was local PAC at the parcel of the LF oscillation and AC of the HF time series.

To assess the fractions of excluded edges, we computed K_{corr} as the fraction of the remaining significant edges divided by number of possible connections after removing all putatively spurious connections.

XIV. Estimation of peak alpha frequency and correlation with the cross-frequency ratio in SEEG data

In order to determine the peak alpha frequency in SEEG phase-amplitude, of SEEG PAC, we interpolated the values of group-level connection density K in the range 6-20 Hz with a cubic function, using the Python package scipy, at a resolution of 0.1 Hz and located the frequency at which the interpolated K value was largest. We then computed Pearson's r as a metric of correlation between CF ratio and peak alpha frequency.

XV. Computation of CFC in distance bins

For both SEEG and MEG data, we divided all channel/parcel pairs into three distance bins containing the same amount of edges. For SEEG data, the distance bins were 2cm – 4cm, 4cm – 5.6cm and 5.6cm – 13.7cm and for MEG data these were 0cm – 6.3cm, 6.3cm – 9.1cm and 9.1cm – 17.7cm. We then computed the K values separately in these distance bins as described above. We tested for significant differences between the first and third bin with a Wilcoxon signed-rank test ($p < 0.05$, corrected for multiple comparisons with Benjamini-Hochberg).

XVI. Estimation of CFC in distinct cortical layers in SEEG data

We assigned SEEG electrode contacts to layers based on the Grey Matter Proximity Index (GMPI) which is the distance between contact position and the nearest vertex of the white-grey surface, normalized by the

cortical thickness in that point (7). Contacts with 0.5 < GMPI < 1.2 were marked as "superficial" and -0.3 < GMPI < 0 as "deep". We analyzed inter-areal CFC among electrode pairs in four groups: 1) where both electrode contacts were in a superficial layer; 2) where both contacts were in a deep layer; 3) where the LF contact was in a superficial and the HF contact in a deep layer; and 4) where the LF contact was in a deep and the HF one in a superficial layer. We tested for significant difference between the group with the largest and the group with the smallest values (groups 1&2 in uncorrected and 3&4 in corrected data) with a Wilcoxon signed-rank test ($p < 0.05$, corrected for multiple comparisons with Benjamini-Hochberg).

XVII. Estimation of relative directed degree

We defined the relative degree per parcel for the 148-parcel Destrieux atlas as the fraction of significant edges N_E connected to a parcel over the total possible number of possible edges $N_{E,pot}$ for that parcel. In SEEG data, $N_{E,pot}$ was obtained by pooling possible CFS or PAC edges over all subjects; for each subject, $N_{E,pot,S}$ was the sum of possible, i.e. not excluded, connections from contacts assigned to that parcel to other electrodes. Parcels with a degree lower than eight were excluded. The relative directed degree was estimated as the difference between in- and out degree, where in-degree was associated with the HF end of a CFC connection, and out-degree with the LF end, so that a positive value indicated a HF hub and a negative value a LF hub. Values were collapsed over all frequencies belonging to the frequency bands of interest.

XVIII. Estimation of CFC directionality

We estimated LF-HF directionality for frequency pairs LF, HF and all parcel pairs ($p_1 \neq p_2$) in the 148-parcel Destrieux atlas.

We defined LF-HF directionality Dir_{LH} as:

$$Dir_{LH}\,(LF, HF, p_1, p_2) = \frac{1}{M}\left(\sum^{M} PLV_{CF}(LF, HF, p_1, p_2) - \sum^{M} PLV_{CF}(LF, HF, p_2, p_1)\right) \quad (5)$$

, where M is the number of connections between the two parcels. In SEEG, where several contacts can be located in one parcel, M for a parcel pair p_1,p_2 is equal to the total number of contact pairs c_1,c_2 in all subjects where c_1 is located in p_1 and c_2 located in p_2. Values for M in SEEG ranged from 0 to 1690. For all pairs (p_1,p_2) in SEEG where M<8, Dir_{LH} was set to 0.

In MEG, where there is exactly one connection between any two parcels in a given set, M was equal to the number of sets.

We then tested for significance for each $Dir_{LH}(LF,HF,p_1,p_2)$ value using a permutation test (N = 1000).

In each permutation, the strengths of all connections $PLV_{CF}(p_1,p_2)$ *and* $PLV_{CF}(p_2,p_1)$ between two parcels p_1,p_2 were pooled and randomly assigned to two groups G_1,G_2. The permutated directionality Dir_{LH} value was then computed as

$$Dir_{LH,perm}\ (LF, HF, p_1, p_2) = \frac{1}{M}\left(\sum^{M} PLV_{CF}(LF, HF, G_1) - \sum^{M} PLV_{CF}(LF, HF, G_2)\right)$$

If the the true Dir_{LH} value was larger than $Dir_{LH,\ perm}$ in 95% of permutations, the connection was deemed significant. A significant value $Dir_{LH} < 0$ thus indicated that parcel p_1 was dominantly the place of the LF oscillation and p_2 the place of the HF oscillation, and vice versa for $Dir_{LH} > 0$.

The overall directionality $Dir_{LH}(p)$of a parcel p was computed as the number of its significantly positive DLH values with other parcels minus the number of its significantly negative DLH values with other parcels, divided by the number of possible connections with other parcels. Thus, similar to the degree-based hubness, a positive or negative value of $Dir_{LH}(p)$ indicated a parcel dominated by the HF or LF oscillations, respectively, in inter-areal CFC. Values were collapsed over all frequencies belonging to the frequency bands of interest.

Reference List

(1) Singer W. Neuronal synchrony: a versatile code for the definition of relations? Neuron 1999 Sep;24(1):49-65, 111-25.

(2) Fries P. A mechanism for cognitive dynamics: neuronal communication through neuronal coherence. Trends Cogn Sci 2005 Oct;9(10):474-480.

(3) Segonne F, Dale AM, Busa E, Glessner M, Salat D, Hahn HK, et al. A hybrid approach to the skull stripping problem in MRI. Neuroimage 2004 Jul;22(3):1060-1075.

(4) Palva JM, Palva S, Kaila K. Phase synchrony among neuronal oscillations in the human cortex. J Neurosci 2005 Apr 13;25(15):3962-3972.

(5) Marzetti L, Della Penna S, Snyder AZ, Pizzella V, Nolte G, de Pasquale F, et al. Frequency specific interactions of MEG resting state activity within and across brain networks as revealed by the multivariate interaction measure. Neuroimage 2013 Apr 28.

(6) Di Lorenzo G, Daverio A, Ferrentino F, Santarnecchi E, Ciabattini F, Monaco L, et al. Altered resting-state EEG source functional connectivity in schizophrenia: the effect of illness duration. Frontiers in Human Neuroscience 2015 04/11;9:234.

(7) Arnulfo G, Hirvonen J, Nobili L, Palva S, Palva JM. Phase and amplitude correlations in resting-state activity in human stereotactical EEG recordings. Neuroimage 2015 Feb 24;112:114-127.

(8) Nikulin VV, Brismar T. Phase synchronization between alpha and beta oscillations in the human electroencephalogram. Neuroscience 2006;137(2):647-657.

(9) Uhlhaas PJ, Pipa G, Lima B, Melloni L, Neuenschwander S, Nikolic D, et al. Neural synchrony in cortical networks: history, concept and current status. Front Integr Neurosci 2009;3:17.

(10) Palva JM, Monto S, Kulashekhar S, Palva S. Neuronal synchrony reveals working memory networks and predicts individual memory capacity. Proc Natl Acad Sci U S A 2010 Apr 20;107(16):7580-7585.

(11) Harris AZ, Gordon JA. Long-range neural synchrony in behavior. Annu Rev Neurosci 2015;38:171-94.

(12) Lobier M, Palva JM, Palva S. High-alpha band synchronization across frontal, parietal and visual cortex mediates behavioral and neuronal effects of visuospatial attention. Neuroimage 2017 Oct 23;165:222-237.

(13) Hirvonen J, Wibral M, Palva JM, Singer W, Uhlhaas P, Palva S. Whole-Brain Source-Reconstructed MEG-Data Reveal Reduced Long-Range Synchronization in Chronic Schizophrenia. eNeuro 2017 Oct 17;4(5):10.1523/ENEURO.0338-17.2017. eCollection 2017 Sep-Oct.

(14) Hirvonen J, Monto S, Wang S, Palva J, Palva S. Dynamic large-scale network synchronization from perception to action. Network Neuroscience 2018.

(15) Sadaghiani S, Hesselmann G, Friston KJ, Kleinschmidt A. The relation of ongoing brain activity, evoked neural responses, and cognition. Front Syst Neurosci 2010 Jun 23;4:20.

(16) Raichle ME, MacLeod AM, Snyder AZ, Powers WJ, Gusnard DA, Shulman GL. A default mode of brain function. Proc Natl Acad Sci U S A 2001 Jan 16;98(2):676-682.

(17) Fox MD, Snyder AZ, Vincent JL, Corbetta M, Van Essen DC, Raichle ME. The human brain is intrinsically organized into dynamic, anticorrelated functional networks. Proc Natl Acad Sci U S A 2005 Jul 5;102(27):9673-9678.

(18) Sadaghiani S, Scheeringa R, Lehongre K, Morillon B, Giraud AL, Kleinschmidt A. Intrinsic connectivity networks, alpha oscillations, and tonic alertness: a simultaneous electroencephalography/functional magnetic resonance imaging study. J Neurosci 2010 Jul 28;30(30):10243-10250.

(19) Hipp JF, Siegel M. BOLD fMRI Correlation Reflects Frequency-Specific Neuronal Correlation. Curr Biol 2015 May 18;25(10):1368-1374.

(20) Palva S, Palva JM. New vistas for alpha-frequency band oscillations. Trends Neurosci 2007 Apr;30(4):150-158.

(21) Buschman TJ, Miller EK. Top-down versus bottom-up control of attention in the prefrontal and posterior parietal cortices. Science 2007 Mar 30;315(5820):1860-1862.

(22) Bastos AM, Vezoli J, Bosman CA, Schoffelen JM, Oostenveld R, Dowdall JR, et al. Visual Areas Exert Feedforward and Feedback Influences through Distinct Frequency Channels. Neuron 2015 Jan 21;85(2):390-401.

(23) Jensen O, Bonnefond M, Marshall TR, Tiesinga P. Oscillatory mechanisms of feedforward and feedback visual processing. Trends Neurosci 2015;38(4):192-194.

(24) Palva S, Palva JM. Functional roles of alpha-band phase synchronization in local and large-scale cortical networks. Front Psychol 2011;2:204.

(25) Vanhatalo S, Palva JM, Holmes MD, Miller JW, Voipio J, Kaila K. Infraslow oscillations modulate excitability and interictal epileptic activity in the human cortex during sleep. Proc Natl Acad Sci U S A 2004 Apr 6;101(14):5053-5057.

(26) Lakatos P, Shah AS, Knuth KH, Ulbert I, Karmos G, Schroeder CE. An oscillatory hierarchy controlling neuronal excitability and stimulus processing in the auditory cortex. J Neurophysiol 2005 Sep;94(3):1904-1911.

(27) Canolty RT, Edwards E, Dalal SS, Soltani M, Nagarajan SS, Kirsch HE, et al. High gamma power is phase-locked to theta oscillations in human neocortex. Science 2006 Sep 15;313(5793):1626-1628.

(28) Axmacher N, Henseler MM, Jensen O, Weinreich I, Elger CE, Fell J. Cross-frequency coupling supports multi-item working memory in the human hippocampus. Proc Natl Acad Sci U S A 2010 Feb 16;107(7):3228-3233.

(29) Roux F, Wibral M, Singer W, Aru J, Uhlhaas PJ. The Phase of Thalamic Alpha Activity Modulates Cortical Gamma-Band Activity: Evidence from Resting-State MEG Recordings. J Neurosci 2013 11/06;33(45):17827.

(30) Lakatos P, Musacchia G, O'Connel MN, Falchier AY, Javitt DC, Schroeder CE. The spectrotemporal filter mechanism of auditory selective attention. Neuron 2013 Feb 20;77(4):750-761.

(31) Park H, Ince RA, Schyns PG, Thut G, Gross J. Frontal top-down signals increase coupling of auditory low-frequency oscillations to continuous speech in human listeners. Curr Biol 2015 Jun 15;25(12):1649-1653.

(32) Park H, Lee DS, Kang E, Kang H, Hahm J, Kim JS, et al. Formation of visual memories controlled by gamma power phase-locked to alpha oscillations. Sci Rep 2016 Jun 16;6:28092.

(33) Keitel A, Gross J, Kayser C. Perceptually relevant speech tracking in auditory and motor cortex reflects distinct linguistic features. PLoS Biol 2018 Mar 12;16(3):e2004473.

(34) Bahramisharif A, Jensen O, Jacobs J, Lisman J. Serial representation of items during working memory maintenance at letter-selective cortical sites. PLoS Biol 2018 Aug 15;16(8):e2003805.

(35) Tass P, Rosenblum MG, Weule J, Kurths J, Pikovsky A, Volkmann J, et al. Detection of n : m phase locking from noisy data: Application to magnetoencephalography. Phys Rev Lett 1998 OCT 12;81(15):3291-3294.

(36) Sauseng P, Klimesch W, Gruber WR, Birbaumer N. Cross-frequency phase synchronization: a brain mechanism of memory matching and attention. Neuroimage 2008 Mar 1;40(1):308-317.

(37) Besle J, Schevon CA, Mehta AD, Lakatos P, Goodman RR, McKhann GM, et al. Tuning of the human neocortex to the temporal dynamics of attended events. J Neurosci 2011 Mar 2;31(9):3176-3185.

(38) Chaieb L, Leszczynski M, Axmacher N, Hohne M, Elger CE, Fell J. Theta-gamma phase-phase coupling during working memory maintenance in the human hippocampus. Cogn Neurosci 2015 Jun 23:1-9.

(39) Siebenhühner F, Wang SH, Palva JM, Palva S. Cross-frequency synchronization connects networks of fast and slow oscillations during visual working memory maintenance. Elife 2016 Sep 26;5:10.7554/eLife.13451.

(40) Jensen O, Colgin LL. Cross-frequency coupling between neuronal oscillations. Trends in Cognitive Sciences 2007 /7;11(7):267-269.

(41) Schroeder CE, Lakatos P. Low-frequency neuronal oscillations as instruments of sensory selection. Trends Neurosci 2009 Jan;32(1):9-18.

(42) Canolty RT, Knight RT. The functional role of cross-frequency coupling. Trends Cogn Sci 2010 Nov;14(11):506-515.

(43) Fell J, Axmacher N. The role of phase synchronization in memory processes. Nat Rev Neurosci 2011 Feb;12(2):105-118.

(44) Palva S, Palva JM. Discovering oscillatory interaction networks with M/EEG: challenges and breakthroughs. Trends Cogn Sci 2012 Apr;16(4):219-230.

(45) Lisman JE, Jensen O. The theta-gamma neural code. Neuron 2013 Mar 20;77(6):1002-1016.

(46) Roux F, Uhlhaas PJ. Working memory and neural oscillations: alpha-gamma versus theta-gamma codes for distinct WM information? Trends Cogn Sci 2014 Jan;18(1):16-25.

(47) Hyafil A, Giraud AL, Fontolan L, Gutkin B. Neural Cross-Frequency Coupling: Connecting Architectures, Mechanisms, and Functions. Trends Neurosci 2015 Nov;38(11):725-740.

(48) Palva JM, Palva S. Functional integration across oscillation frequencies by cross-frequency phase synchronization. Eur J Neurosci 2017 11/02; 2018/04;0(0).

(49) Tort AB, Kramer MA, Thorn C, Gibson DJ, Kubota Y, Graybiel AM, et al. Dynamic cross-frequency couplings of local field potential oscillations in rat striatum and hippocampus during performance of a T-maze task. Proc Natl Acad Sci U S A 2008 Dec 23;105(51):20517-20522.

(50) Roopun AK, Kramer MA, Carracedo LM, Kaiser M, Davies CH, Traub RD, et al. Period concatenation underlies interactions between gamma and beta rhythms in neocortex. Front Cell Neurosci 2008;2:1.

(51) Tort AB, Komorowski R, Eichenbaum H, Kopell N. Measuring phase-amplitude coupling between neuronal oscillations of different frequencies. J Neurophysiol 2010 Aug;104(2):1195-1210.

(52) Belluscio MA, Mizuseki K, Schmidt R, Kempter R, Buzsaki G. Cross-frequency phase-phase coupling between theta and gamma oscillations in the hippocampus. J Neurosci 2012 Jan 11;32(2):423-435.

(53) Scheffer-Teixeira R, Belchior H, Caixeta F, Souza BC, Ribeiro S, Tort ABL. Theta Phase Modulates Multiple Layer-Specific Oscillations in the CA1 Region. Cerebral Cortex 2012 10/01;22(10):2404-2414.

(54) Xu X, Zheng C, Zhang T. Reduction in LFP cross-frequency coupling between theta and gamma rhythms associated with impaired STP and LTP in a rat model of brain ischemia. Frontiers in Computational Neuroscience 2013 03/17;7:27.

(55) Scheffer-Teixeira R, Tort ABL. Unveiling Fast Field Oscillations through Comodulation. eNeuro 2017 Aug 4;4(4):10.1523/ENEURO.0079-17.2017. eCollection 2017 Jul-Aug.

(56) Jiang H, Bahramisharif A, van Gerven MAJ, Jensen O. Measuring directionality between neuronal oscillations of different frequencies. NeuroImage 2015 September 2015;118:359-367.

(57) Watrous AJ, Deuker L, Fell J, Axmacher N. Phase-amplitude coupling supports phase coding in human ECoG. Elife 2015 Aug 26;4:10.7554/eLife.07886.

(58) Berman JI, Liu S, Bloy L, Blaskey L, Roberts TPL, Edgar JC. Alpha-to-Gamma Phase-Amplitude Coupling Methods and Application to Autism Spectrum Disorder. Brain Connectivity 2015 04/01;5(2):80-90.

(59) Jirsa V, Muller V. Cross-frequency coupling in real and virtual brain networks. Front Comput Neurosci 2013 Jul 3;7:78.

(60) Sauseng P, Klimesch W, Heise KF, Gruber WR, Holz E, Karim AA, et al. Brain oscillatory substrates of visual short-term memory capacity. Curr Biol 2009 Nov 17;19(21):1846-1852.

(61) Akiyama M, Tero A, Kawasaki M, Nishiura Y, Yamaguchi Y. Theta-alpha EEG phase distributions in the frontal area for dissociation of visual and auditory working memory. Sci Rep 2017 Mar 7;7:42776.

(62) Zheng C, Zhang T. Alteration of phase-phase coupling between theta and gamma rhythms in a depression-model of rats. Cognitive Neurodynamics 2013 04/01;7(2):167-172.

(63) Isler JR, Grieve PG, Czernochowski D, Stark RI, Friedman D. Cross-frequency phase coupling of brain rhythms during the orienting response. Brain Res 2008 9/26;1232(0):163-172.

(64) Florin E, Baillet S. The brain's resting-state activity is shaped by synchronized cross-frequency coupling of neural oscillations. Neuroimage 2015 May 1;111:26-35.

(65) van der Meij R, Kahana M, Maris E. Phase-amplitude coupling in human electrocorticography is spatially distributed and phase diverse. J Neurosci 2012 Jan 4;32(1):111-123.

(66) Kramer MA, Tort ABL, Kopell NJ. Sharp edge artifacts and spurious coupling in EEG frequency comodulation measures. J Neurosci Methods 2008 05/30;170(2):352-357.

(67) Aru J, Aru J, Priesemann V, Wibral M, Lana L, Pipa G, et al. Untangling cross-frequency coupling in neuroscience. Curr Opin Neurobiol 2015 Apr;31:51-61.

(68) van Driel J, Cox R, Cohen MX. Phase-clustering bias in phase–amplitude cross-frequency coupling and its removal. Journal of Neuroscience Methods 2015 30 October 2015;254:60-72.

(69) Gerber EM, Sadeh B, Ward A, Knight RT, Deouell LY. Non-Sinusoidal Activity Can Produce Cross-Frequency Coupling in Cortical Signals in the Absence of Functional Interaction between Neural Sources. PLoS One 2016 Dec 12;11(12):e0167351.

(70) Scheffer-Teixeira R, Tort AB. On cross-frequency phase-phase coupling between theta and gamma oscillations in the hippocampus. Elife 2016 Dec 7;5:10.7554/eLife.20515.

(71) Lozano-Soldevilla D, Ter Huurne N, Oostenveld R. Neuronal Oscillations with Non-sinusoidal Morphology Produce Spurious Phase-to-Amplitude Coupling and Directionality. Front Comput Neurosci 2016 Aug 22;10:87.

(72) Cole SR, Voytek B. Brain Oscillations and the Importance of Waveform Shape. Trends Cogn Sci 2017 Feb;21(2):137-149.

(73) Nikulin VV, Linkenkaer-Hansen K, Nolte G, Lemm S, Muller KR, Ilmoniemi RJ, et al. A novel mechanism for evoked responses in the human brain. Eur J Neurosci 2007 May;25(10):3146-3154.

(74) Destrieux C, Fischl B, Dale A, Halgren E. Automatic parcellation of human cortical gyri and sulci using standard anatomical nomenclature. Neuroimage 2010 Oct 15;53(1):1-15.

(75) Muthukumaraswamy SD. High-frequency brain activity and muscle artifacts in MEG/EEG: a review and recommendations. Frontiers in Human Neuroscience 2013 03/28;7:138.

(76) Vinck M, Oostenveld R, van Wingerden M, Battaglia F, Pennartz CM. An improved index of phase-synchronization for electrophysiological data in the presence of volume-conduction, noise and sample-size bias. Neuroimage 2011 Apr 15;55(4):1548-1565.

(77) Palva JM, Wang SH, Palva S, Zhigalov A, Monto S, Brookes MJ, et al. Ghost interactions in MEG/EEG source space: A note of caution on inter-areal coupling measures. NeuroImage 2018 June 2018;173:632-643.

(78) Bassett DS, Bullmore E. Small-world brain networks. Neuroscientist 2006 Dec;12(6):512-523.

(79) Yeo BT, Krienen FM, Sepulcre J, Sabuncu MR, Lashkari D, Hollinshead M, et al. The organization of the human cerebral cortex estimated by intrinsic functional connectivity. J Neurophysiol 2011 Sep;106(3):1125-1165.

(80) Ciuciu P, Varoquaux G, Abry P, Sadaghiani S, Kleinschmidt A. Scale-free and multifractal properties of fMRI signals during rest and task. Frontiers in Physiology 2012;3:186.

(81) Raichle ME. The Brain's Default Mode Network. Annu Rev Neurosci 2015 07/08; 2018/12;38(1):433-447.

(82) Zhigalov A, Arnulfo G, Nobili L, Palva S, Palva JM. Modular co-organization of functional connectivity and scale-free dynamics in the human brain. Network Neuroscience 2017;1.

(83) Demiralp T, Bayraktaroglu Z, Lenz D, Junge S, Busch NA, Maess B, et al. Gamma amplitudes are coupled to theta phase in human EEG during visual perception. Int J Psychophysiol 2007 Apr;64(1):24-30.

(84) Berger H. Uber das elektroenkephalogramm des Menschen. Arch Psychiatr Nervenkr 1929;87:527-570.

(85) Klimesch W, Sauseng P, Hanslmayr S. EEG alpha oscillations: the inhibition-timing hypothesis. Brain Res Rev 2007 Jan;53(1):63-88.

(86) Palva JM, Palva S. Roles of multiscale brain activity fluctuations in shaping the variability and dynamics of psychophysical performance. Prog Brain Res 2011;193:335-350.

(87) Klimesch W. Alpha-band oscillations, attention, and controlled access to stored information. Trends Cogn Sci 2012 Dec;16(12):606-617.

(88) Corbetta M, Shulman GL. Control of goal-directed and stimulus-driven attention in the brain. Nat Rev Neurosci 2002 Mar;3(3):201-215.

(89) Larsson P, Kostov H. Lower frequency variability in the alpha activity in EEG among patients with epilepsy. Clinical Neurophysiology 2005 2018/04;116(11):2701-2706.

(90) Stein Av, Chiang C, Konig P. Top-down processing mediated by interareal synchronization. Proc Natl Acad Sci U S A 2000 Dec 19;97(26):14748-14753.

(91) Bollimunta A, Chen Y, Schroeder CE, Ding M. Neuronal mechanisms of cortical alpha oscillations in awake-behaving macaques. J Neurosci 2008 Oct 1;28(40):9976-9988.

(92) Bollimunta A, Mo J, Schroeder CE, Ding M. Neuronal mechanisms and attentional modulation of corticothalamic alpha oscillations. J Neurosci 2011 Mar 30;31(13):4935-4943.

(93) Haegens S, Barczak A, Musacchia G, Lipton ML, Mehta AD, Lakatos P, et al. Laminar Profile and Physiology of the alpha Rhythm in Primary Visual, Auditory, and Somatosensory Regions of Neocortex. J Neurosci 2015 Oct 21;35(42):14341-14352.

(94) Halgren M, Fabo D, Ulbert I, Madsen JR, Eross L, Doyle WK, et al. Superficial Slow Rhythms Integrate Cortical Processing in Humans. Scientific Reports 2018 02/01;8(1):2055.

(95) Arnulfo G, Narizzano M, Cardinale F, Fato MM, Palva JM. Automatic segmentation of deep intracerebral electrodes in computed tomography scans. BMC Bioinformatics 2015 Mar 25;16(1):99-015-0511-6.

(96) Buffalo EA, Fries P, Landman R, Buschman TJ, Desimone R. Laminar differences in gamma and alpha coherence in the ventral stream. Proc Natl Acad Sci U S A 2011 Jul 5;108(27):11262-11267.

(97) Dosenbach NU, Fair DA, Miezin FM, Cohen AL, Wenger KK, Dosenbach RA, et al. Distinct brain networks for adaptive and stable task control in humans. Proc Natl Acad Sci U S A 2007 Jun 26;104(26):11073-11078.

(98) Sauseng P, Klimesch W, Schabus M, Doppelmayr M. Fronto-parietal EEG coherence in theta and upper alpha reflect central executive functions of working memory. Int J Psychophysiol 2005 Aug;57(2):97-103.

(99) Vidal JR, Chaumon M, O'Regan JK, Tallon-Baudry C. Visual grouping and the focusing of attention induce gamma-band oscillations at different frequencies in human magnetoencephalogram signals. J Cogn Neurosci 2006 Nov;18(11):1850-1862.

(100) Rouhinen S, Panula J, Palva JM, Palva S. Load dependence of beta and gamma oscillations predicts individual capacity of visual attention. J Neurosci 2013 Nov 27;33(48):19023-19033.

(101) Honkanen R, Rouhinen S, Wang SH, Palva JM, Palva S. Gamma Oscillations Underlie the Maintenance of Feature-Specific Information and the Contents of Visual Working Memory. Cereb Cortex 2015 Oct;25(10):3788-3801.

(102) Michalareas G, Vezoli J, van Pelt S, Schoffelen J, Kennedy H, Fries P. Alpha-Beta and Gamma Rhythms Subserve Feedback and Feedforward Influences among Human Visual Cortical Areas. Neuron 2016.

(103) Jones SR. When brain rhythms aren't 'rhythmic': implication for their mechanisms and meaning. Current Opinion in Neurobiology 2016 October 2016;40:72-80.

(104) Schoffelen JM, Gross J. Source connectivity analysis with MEG and EEG. Hum Brain Mapp 2009 Jun;30(6):1857-1865.

(105) Cardinale F, Cossu M, Castana L, Casaceli G, Schiariti MP, Miserocchi A, et al. Stereoelectroencephalography: surgical methodology, safety, and stereotactic application accuracy in 500 procedures. Neurosurgery 2013 Mar;72(3):353-66; discussion 366.

(106) Narizzano M, Arnulfo G, Ricci S, Toselli B, Tisdall M, Canessa A, et al. SEEG assistant: a 3DSlicer extension to support epilepsy surgery. - BMC Bioinformatics 2017(18):124.

(107) Tallon-Baudry C, Bertrand O, Delpuech C, Pernier J. Stimulus specificity of phase-locked and non-phase-locked 40 Hz visual responses in human. J Neurosci 1996 Jul 1;16(13):4240-4249.

(108) Taulu S, Simola J. Spatiotemporal signal space separation method for rejecting nearby interference in MEG measurements. Phys Med Biol 2006 Apr 7;51(7):1759-1768.

(109) Oostenveld R, Fries P, Maris E, Schoffelen JM. FieldTrip: Open source software for advanced analysis of MEG, EEG, and invasive electrophysiological data. Comput Intell Neurosci 2011;2011:156869.

(110) Dale AM, Fischl B, Sereno MI. Cortical surface-based analysis. I. Segmentation and surface reconstruction. Neuroimage 1999 Feb;9(2):179-194.

(111) Fischl B, Salat DH, Busa E, Albert M, Dieterich M, Haselgrove C, et al. Whole brain segmentation: automated labeling of neuroanatomical structures in the human brain. Neuron 2002 Jan 31;33(3):341-355.

(112) Korhonen O, Palva S, Palva JM. Sparse weightings for collapsing inverse solutions to cortical parcellations optimize M/EEG source reconstruction accuracy. J Neurosci Methods 2014 Feb 6;226C:147-160.

(113) Dale AM, Liu AK, Fischl BR, Buckner RL, Belliveau JW, Lewine JD, et al. Dynamic statistical parametric mapping: combining fMRI and MEG for high-resolution imaging of cortical activity. Neuron 2000 Apr;26(1):55-67.

(114) Gramfort A, Luessi M, Larson E, Engemann DA, Strohmeier D, Brodbeck C, et al. MNE software for processing MEG and EEG data. Neuroimage 2014;86:446-460.

(115) Wang S, Lobier L, Siebenhühner F, Puoliväli T, Palva S, Palva J. Hyperedge bundling: A practical solution to spurious interactions in MEG/EEG connectivity analyses. NeuroImage 2018;S1053-8119(18):0056.

Suppl. Figure Legends

S1 Figure. Workflow for SEEG data

Workflow for the processing and analysis of SEEG data, flowing from top to bottom.

S2 Figure. Workflow for MEG data

Workflow for the processing and analysis of MEG data, flowing from top to bottom.

S3 Figure. Example of CFS in SEEG data

Cross-frequency phase synchrony (CFS) between two electrode contacts, whose location is indicated by big blue and red circles on the anatomical image of a participant's brain (left). The small circles indicates the positions of closest white matter contacts. *Top row*: Broadband signal (black line) recorded from a contact in the medial frontal gyrus (MFG), and the narrow-band signal (blue) at 9Hz. *2nd row*: Broadband signal (black) recorded from a contact in the intraparietal sulcus (IPS), and the narrowband signal (red) at 27Hz. *3rd row*: The instantaneous phases of the narrowband MfG 9Hz signal (top), the same phase multiplied with 3 (middle) and of the IPS 27Hz signal. *Bottom row*: The 1:3 PLV (purple), indicating the strength of CFS coupling between the 9Hz and the 27Hz signal, and the 95th %ile of 1:3 PLV values for surrogate data (grey dashed line).

S4 Figure. Example of PAC in MEG data

Phase-amplitude coupling (PAC) between source-reconstructed signals in the postcentral gyrus (poCG) and superior temporal sulcus (sTS), as shown on a template brain pial surface (left). *Top row*: Broadband signal (black line) and 10Hz narrowband signal (blue) at poCG. *Second row*: Broadband signal (black) and 40Hz narrowband signal (red) at sTS. *Third row*: Narrowband signals at 10 Hz and 40 Hz with the frequency ratio of 1:4. Starting at around 200ms, the amplitude of the HF signal at 40 Hz starts being modulated by the phase of the 10 Hz LF signal. *Bottom row*: Strength of 1:4 PAC coupling (purple) and the 95th %ile of surrogate values obtained by phase shifting (grey dashed line).

S5 Figure. 1:1 phase synchrony in SEEG and MEG

a) Phase synchrony mean strength (top) and connection density *K* (bottom) in SEEG data with 95% confidence limits estimated with the weighted Phase-Lag Index (wPLI) overall (left) and separately in three distance bins containing equal numbers of connections (right). **b)** Phase synchrony in SEEG data estimated with the Phase-Locking Value (PLV). **c-d)** Phase synchrony in MEG data estimated with wPLI and PLV, respectively.

S6 Figure. Local CFS and PAC in SEEG and MEG data.

a) The mean PLV strength and fraction of significant parcels (*K)* with 95% confidence limits (shaded) of local CFS in SEEG data for coupling ratios 1:2 (top) and 1:3 – 1:7 (bottom). Values are shown with 95% confidence limits. **b)** The mean PLV strength and fraction of significant parcels *K* for local CFS in MEG data. **c)** Same for local PAC in SEEG data. **d)** Same for local PAC in MEG data. **e)-h)** The same *K* values as shown in a-d plotted in matrices for the whole spectral connectome.

S7 Figure. Strength of inter-areal CFS and PAC

The mean strength of inter-areal CFC with 95% confidence limits for ratio 1:2 (top row) and ratios 1:2−1:7 (bottom row), as estimated by the n:m PLV for CFS, or for PAC by the PLV of the LF signal and the phase of the LF-filtered amplitude envelopes of the HF signal.

S8 Figure. Inter-areal CFS and PAC when PLV is used for removing spurious connections

a) Connection density *K* of inter-areal CFS in SEEG data before (left) and after removing possible spurious connections (K_{corr}, right) using the PLV as a metric for phase synchrony. **b)** Same for inter-areal PAC in SEEG data. **c)-d)** Same for inter-areal CFS and PAC in MEG data.

S9 Figure: Amplitude envelope correlations

Mean strength and *K* of synchronization between amplitude envelopes that were modulated by the phase of a lower frequency at a ratio from 1:2 to 1:7. The same data is plotted as a function of the envelope frequency (top row) and the modulating frequency (bottom row).

S10 Figure: Functional Networks

Functional networks of the Yeo parcellation.

S1 Figure

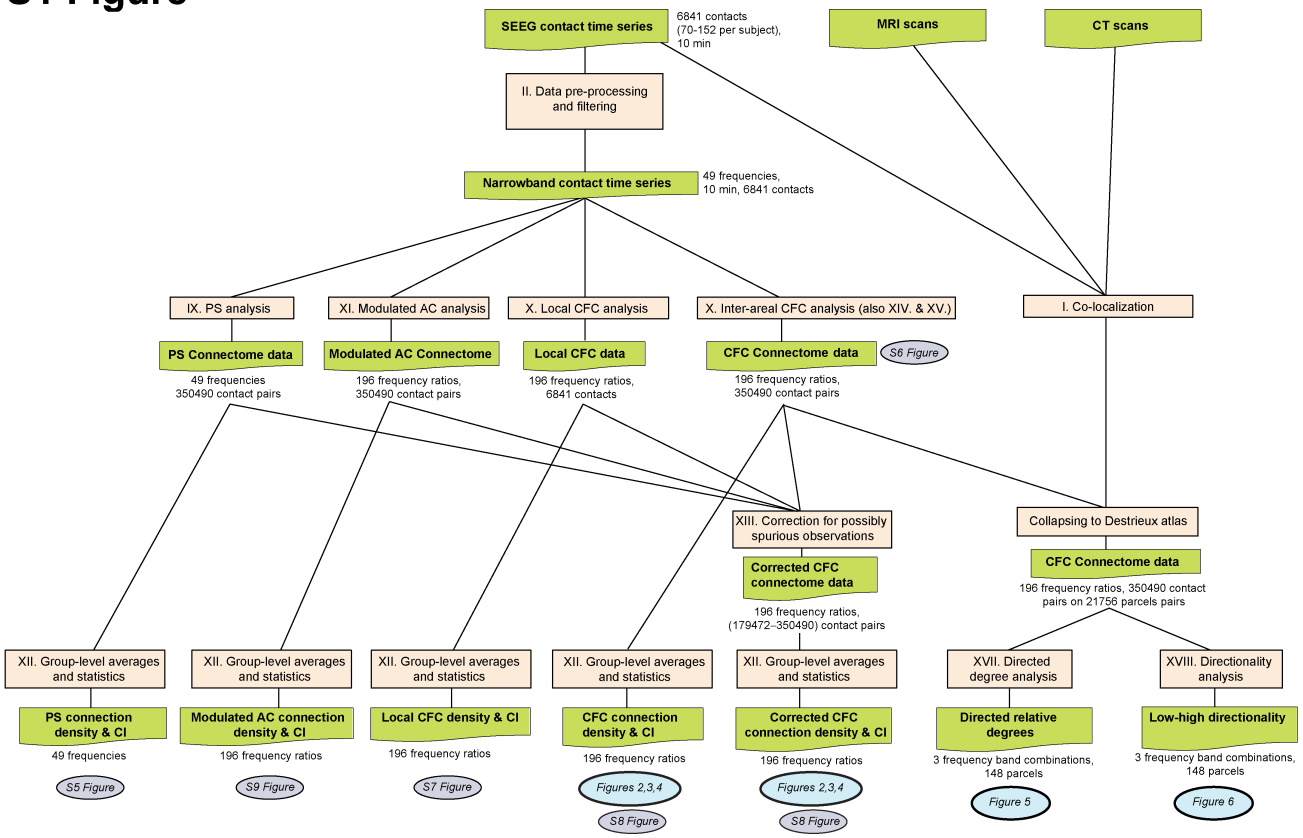

S2 Figure

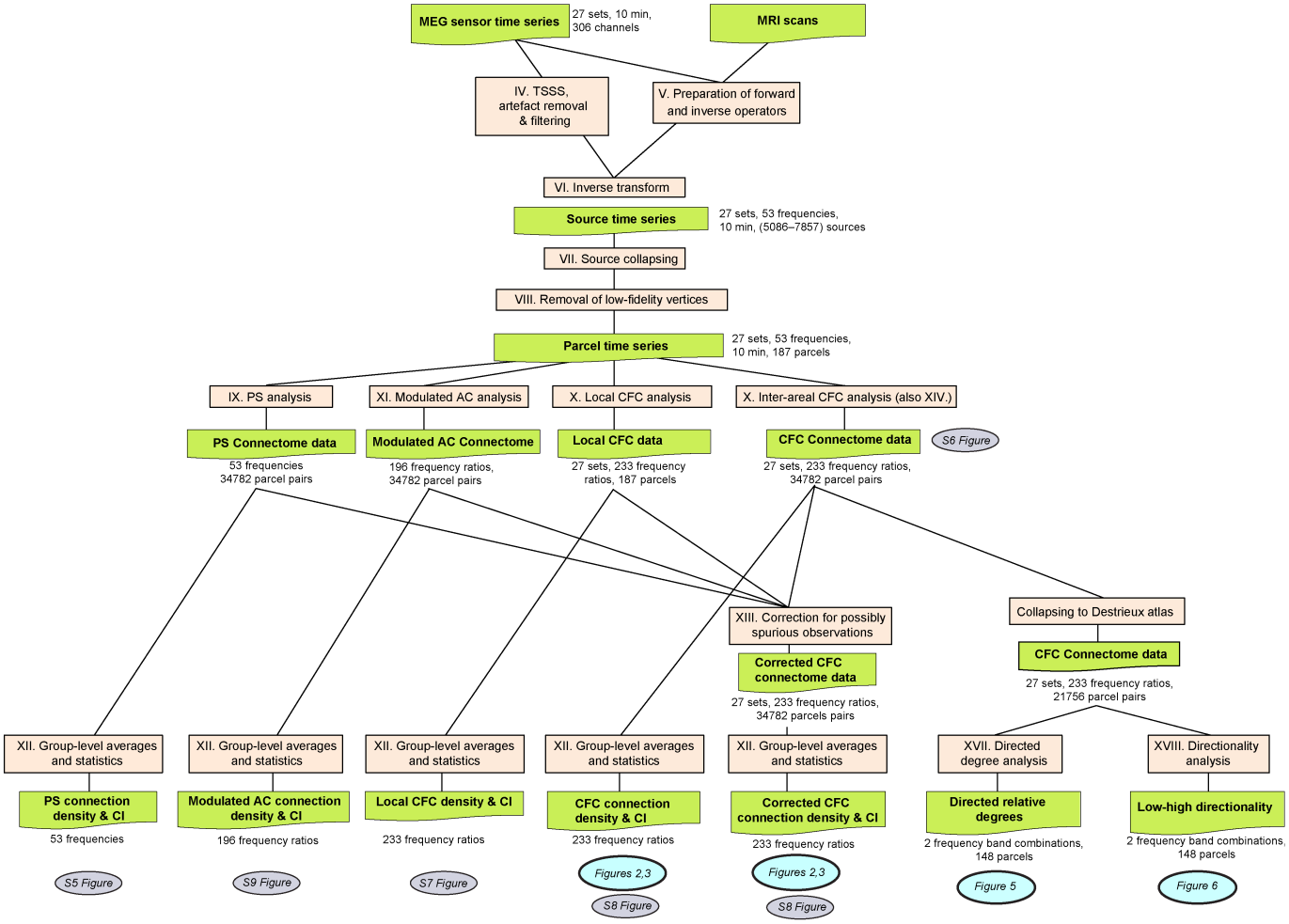

S3 Figure

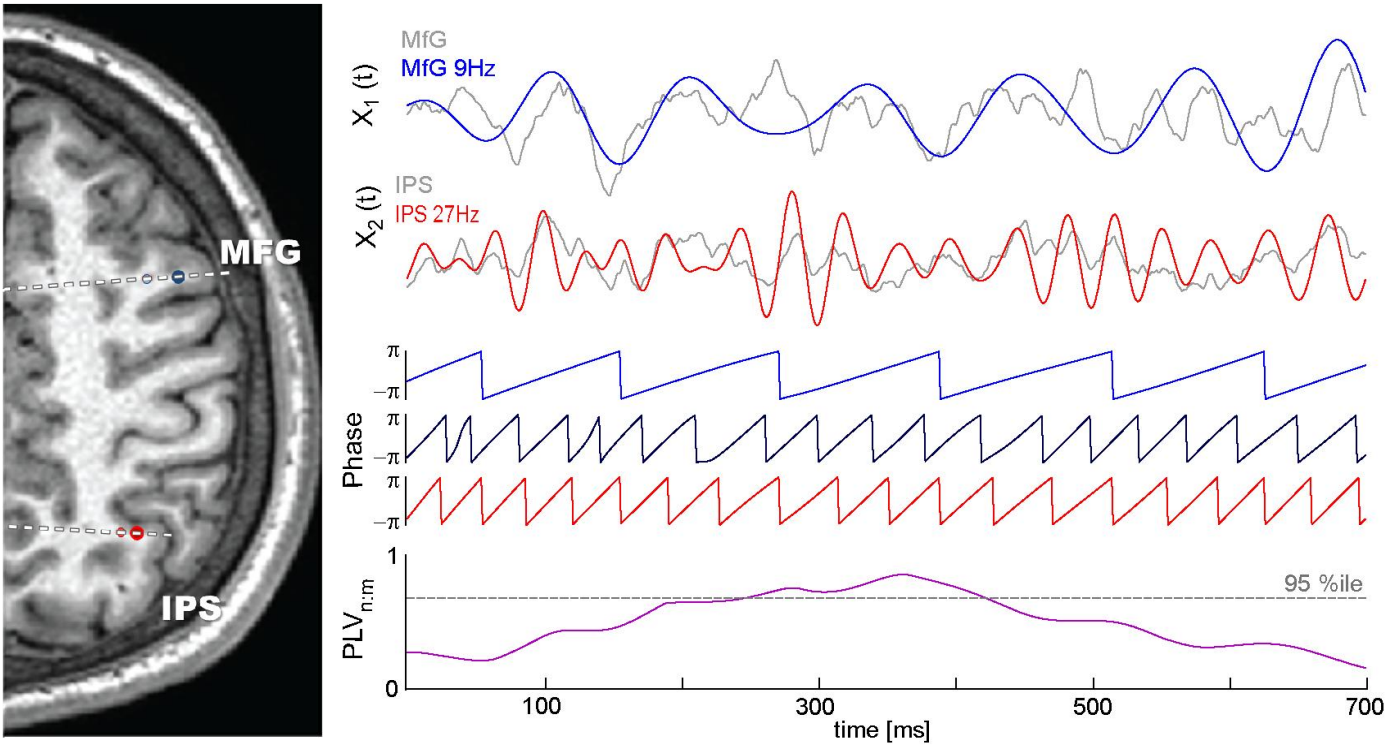

S4 Figure

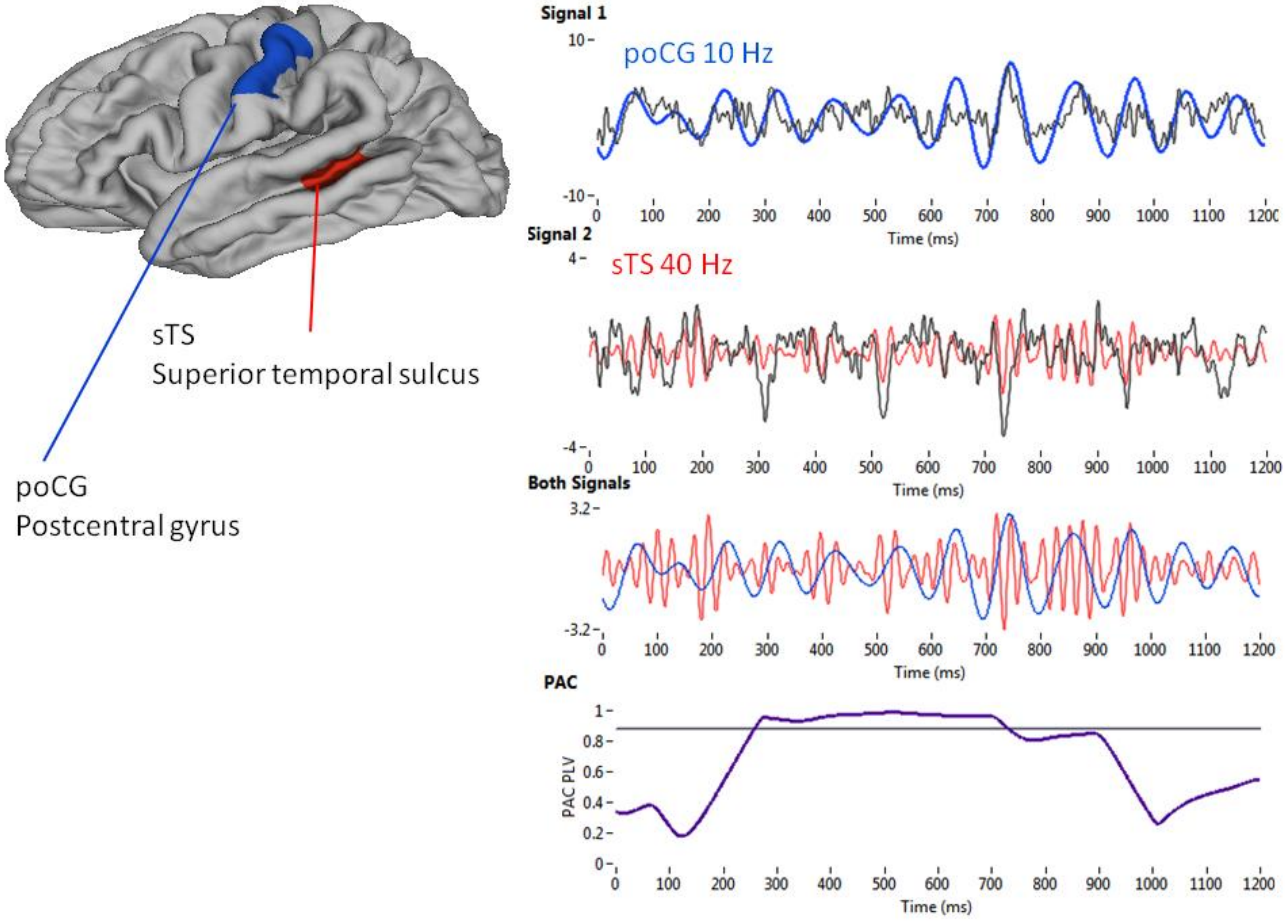

S5 Figure

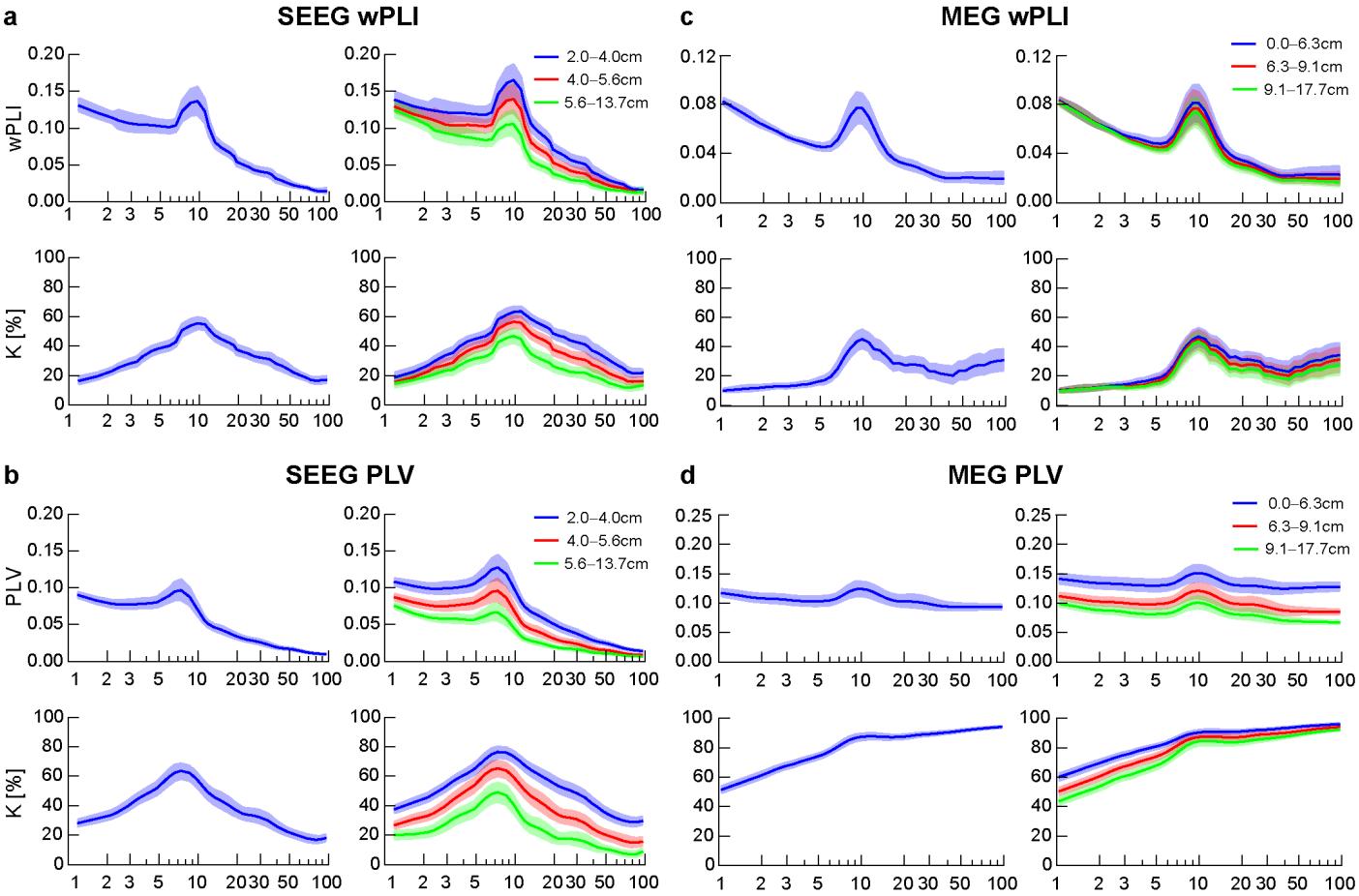

S6 Figure

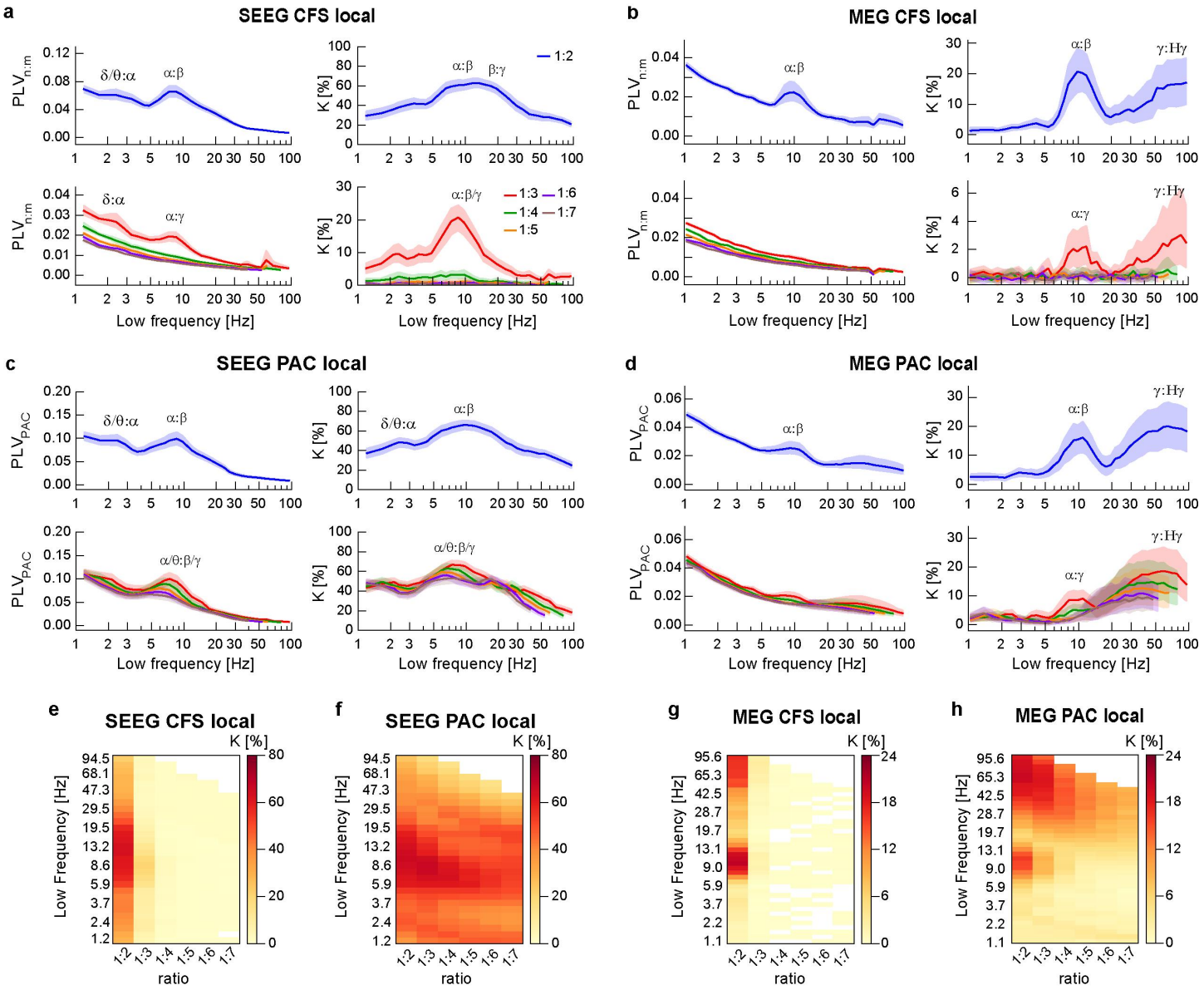

S7 Figure

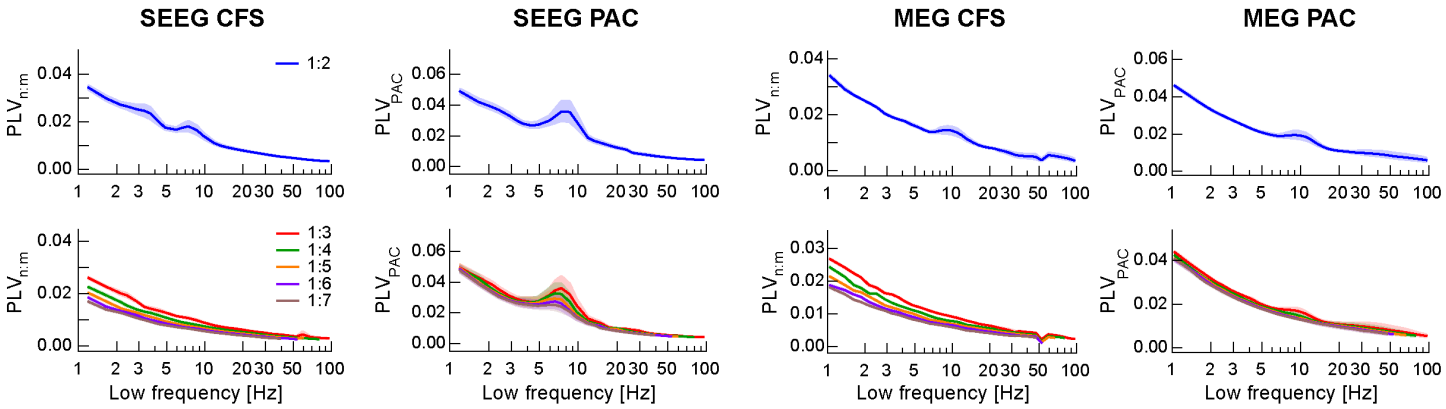

S8 Figure

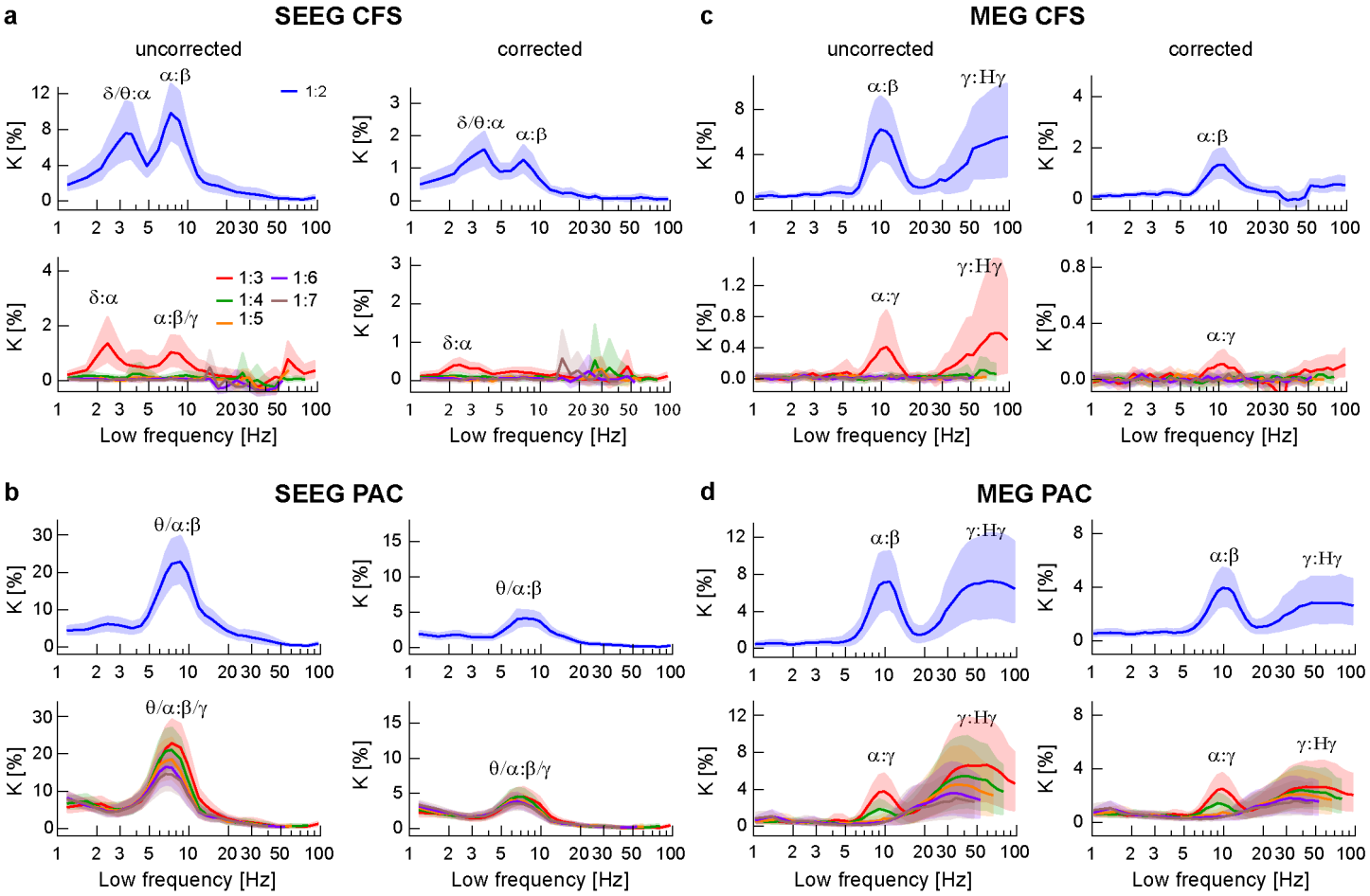

S9 Figure

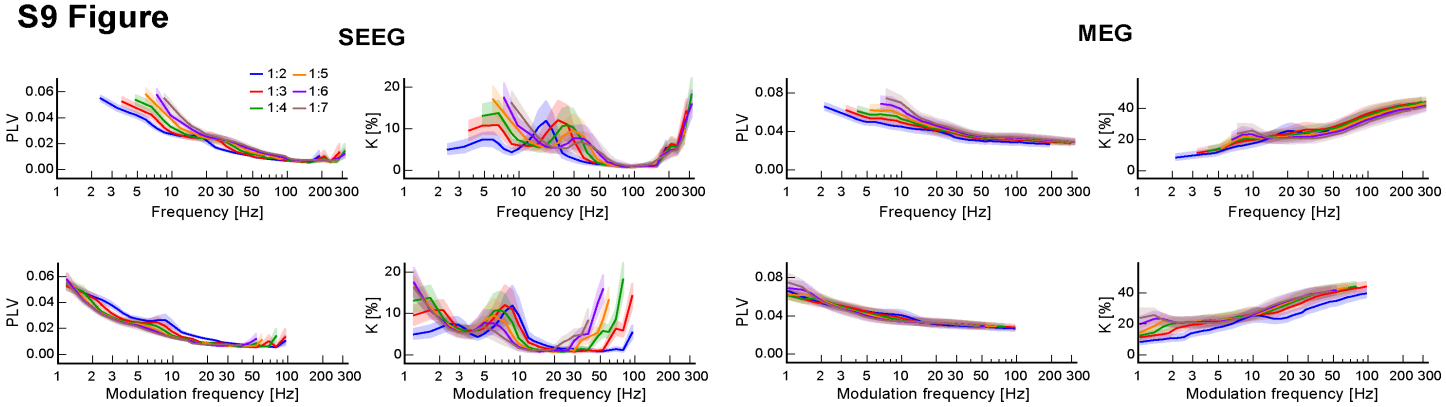

S10 Figure